EMS: Biomedical Sciences
University of Edinburgh
Honours Project

Anatomy and Development
2022-23

Multi-material additive manufacturing to recapitulate the osteotendinous enthesis: an exploration of tensile properties and cytocompatibility.

Laboratory / Clinical Project
4994

[redacted]

[redacted]

[redacted]

[redacted]

[redacted]

[redacted]

[redacted]

[redacted]

[redacted]

[redacted]

[redacted]

[redacted]

Acknowledgments

[redacted] – for her invaluable help with all the cell culture experiments. [redacted] the University of Dundee for letting me use their universal testing machine. [redacted] – for her mathematical support. [redacted] at the IMPACT facility for her epifluorescence microscopy guidance. The Deanery of Biomedical Sciences at the University of Edinburgh for funding this work. Finally, my supervisor [redacted] for her invaluable advice and support throughout this project.

Abbreviations

ABS	Acrylonitrile-co-butadiene-co-styrene	PLA	Poly(lactic) acid
dROb	Differentiated rat osteoblast	sDMEM	Supplemented Dulbeco's modified essential medium
FDM	Fused deposition modelling	STL	Standard tessellation language
FDP	Flexor digitorum profundus	TPE	Thermoplastic elastomer
PBS	Phosphate-buffered saline	TPLA	Tough poly(lactic) acid
PETG	polyethylene terephthalate glycol-modified	TPU	Thermoplastic poly(urethane)

Abstract

Injuries to the attachment site of tendons or ligaments to bones (entheses) are common, such as tennis elbow. The enthesis has a highly complex and organised structure to dissipate the force generated by muscles to the underlying rigid bone without damaging the compliant tendon. However, current repair of these injuries does not recapitulate this architecture and is consequently prone to reinjury. Here, a model of the enthesis is produced using multi-material 3D printing, and its tensile properties evaluated. Three joint types and five materials were evaluated. It was shown that this technique was able to mimic the ultimate tensile strength of the human extensor digitorum brevis tendon. Additionally, cytotoxicity and cell adhesion assays demonstrated the viability of these materials to support osteoblasts *in vitro*. Finally, an anatomically correct scaffold of the distal phalanx and flexor digitorum profundus tendon was produced. Overall, this project has demonstrated a proof-of-concept of a viable technique to develop customisable, anatomically relevant, non-cytotoxic, cell-adhesive scaffolds for entheseal tissue engineering with adequate tensile properties and an interface between rigid and compliant materials.

Lay abstract

Rotator cuff injuries, tennis elbow, jumper's knee and a host of other painful conditions are caused by damage to the site where tendons attach to bone. This area is complex and current treatments lack the ability to fully repair this site. Consequently, repairs are poor, often limiting the range of motion of the joint and reinjury is common. New repair strategies are being investigated in the laboratory to use cells to craft a new tendon-bone attachment, which may then be implanted. Currently, research in this area faces a key problem in combing two materials – hard bone and soft tendon – with such different characteristics. This project uses 3D printing with hard and soft plastics to show that it is possible to mimic the properties of the tendon-bone attachment. Furthermore, these plastics were found to be non-toxic and allow cells to stick to their surfaces. Additionally, an accurate model of a fingertip with its tendon was produced showing the potential of this technique to overcome current issues in this field. Overall, this project demonstrated the feasibility of 3D printing with two materials to replicate the tendon-bone attachment site.

Introduction

The osteoligamentous or osteotendinous interface is known as the enthesis (Benjamin et al., 2002). The interface between these tissues with disparate mechanical properties is key to the function of the appendicular skeleton; without the complex architecture of the enthesis (Figure 1), muscle contraction would inevitably lead to rupture of the tendon attachment site (Apostolakos *et al.*, 2014).

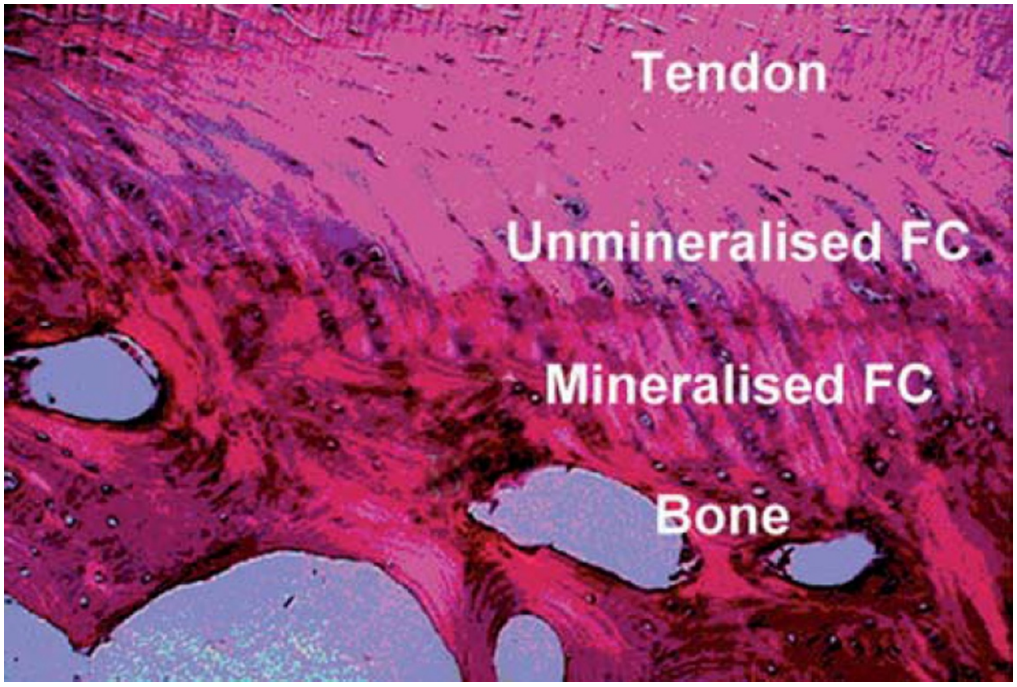

Figure 1. The enthesis showing the complex microarchitecture of this region in the interface between tendon and bone, with both mineralised and unmineralized fibrocartilage (FC) between. Reproduced from Cormick (2010).

Clinically, the enthesis is a relevant area. A wide gamut of common pathologies are directly related to the enthesis. These enthesopathies include jersey finger (Ruchelsman *et al.*, 2011), rotator cuff injuries (Czyrny, 2012), and tennis elbow (Drake and Ring, 2016). Jersey finger is an avulsion fracture of the distal phalanx at the insertion site of the flexor digitorum profundus (FDP) (Figure 2). Classically, the mechanism of injury in jersey finger is a sudden load to the flexed distal fingertip; current repair techniques do not recapitulate the force-modulating properties of the enthesis and hence relapse is common (Ruchelsman *et al.*, 2011).

Figure 2. Jersey finger avulsion fracture of the distal phalanx. The avulsed bone fragment is shown in the white ellipse. Adapted from: Khalilzadeh et al. (2021).

One future treatment option is the fabrication of a custom tissue engineered entheseal graft to replace the damaged region entirely. This would consist of cementing a bone anchor in place of the avulsed fragment, and suturing the free end of the FDP tendon to the tendon of the graft. However, producing a cohesive scaffold with such radically different mechanical properties is a key challenge facing interfacial tissue engineers currently (Vesvoranan *et al.*, 2022).

One potential solution to this problem is to use multi-material 3D printing to combine rigid and compliant materials into one cohesive scaffold structure. The customisability and speed of 3D printing enables rapid iteration of prototyping. Consequently, this technology presents a unique opportunity to carefully control the interface between these two material types and to evaluate their mechanical properties.

The fundamental hypothesis underpinning this project is that multi-material 3D printing is able to produce composite rigid-compliant 3D-printed structures which demonstrate comparable mechanical properties to human entheses. The secondary hypothesis is that these materials are not cytotoxic and will allow the adhesion of relevant cell types.

The aims of this project (Table 1) fall into two categories: firstly, examining the mechanical properties of the composite materials, and secondly examining the cellular response to these materials.

Table 1. Aims of this project for both evaluation of the tensile properties of the composite materials and the cellular work.

Mechanical properties	Cellular responses
Aim 1: Evaluate the feasibility of printing multiple materials together	Aim 4: Assess direct cytotoxicity of printed materials
Aim 2: Examine the differences in tensile properties between joint types	Aim 5: Assess cell viability in media exposed to the materials
Aim 3: Characterise tensile properties of the different composites	Aim 6: Evaluate cell adhesion to the printed materials

Materials and methods

Fused deposition modelling

Fused deposition modelling (FDM) is one technique within additive manufacturing, informally known as 3D printing (Stansbury and Idacavage, 2016). FDM utilises thermoplastic polymer filament as its raw material which is heated and extruded through a nozzle onto a heated plate (Figure 3A). The path the nozzle moves along is controlled by a series of sequential X, Y, and Z moves which are generated by 'slicing' a 3D model into single layers of height *z* (Figure 3B). Repeated stacking of layers of filament on top of each other produces the final three-dimensional object (Figure 3C).

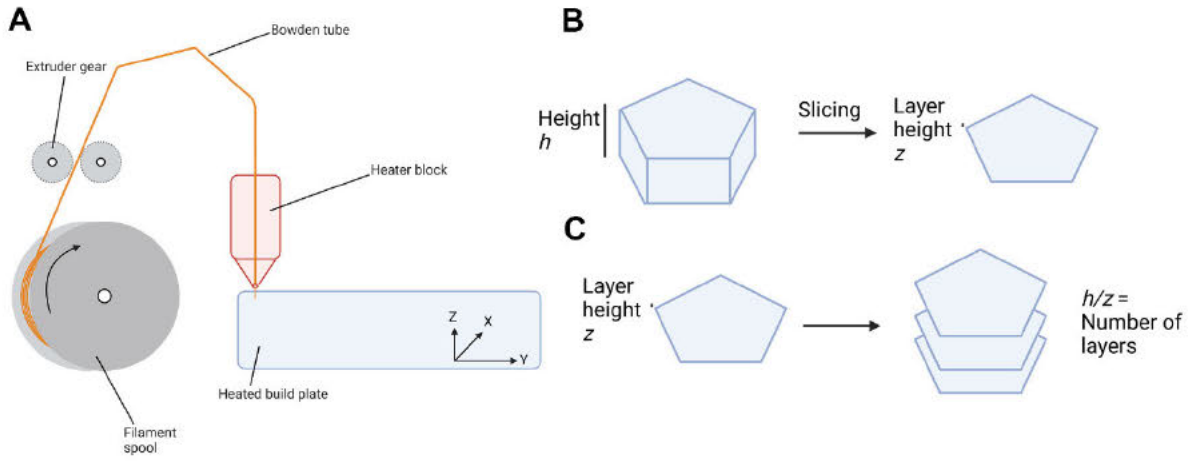

Figure 3. (A) Schematic of fused deposition modelling (FDM) process. (B) Diagram of the 'slicing' process converting a 3D model into a printable object. (C) Illustrating how FDM produces 3D objects by stacking thin layers on top of each other to reach the final object's height.

Production of tensile testing samples

Samples for tensile testing (Figure 4) were designed in Fusion 360 (Autodesk) according to BS EN ISO 527-2:2012 (British Standards Institution, 2012) test specimen type 1A (Table 2). Although a different standard exists for tensile testing of compliant thermoplastics (British Standards Institution, 2017), as the majority of materials used are hard thermoplastics, BS EN ISO 527-2:2012 was used.

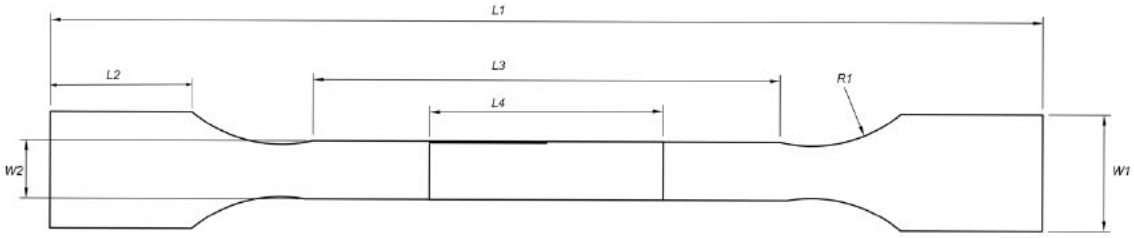

Figure 4. Schematic of tensile samples prepared according to BS EN ISO 527-2:2012.

Table 2. Dimensions of tensile samples.

Dimension	Measurement (mm)
L1 - Overall length	170.00
L2 - Broad section length	24.29
L3 - Narrow section length	80.00
L4 - Overlapping section length	40.00
W1 - Broad section width	20.00
W2 - Narrow section width	10.00
R1 - Broad-narrow transition radius	24.00
Thickness	4.00

To model the interface between tendon and bone three joint types of varying complexity were designed: a butt joint (Figure 5A), a lap joint (Figure 5B), and an interdigitated joint (Figure 5C).

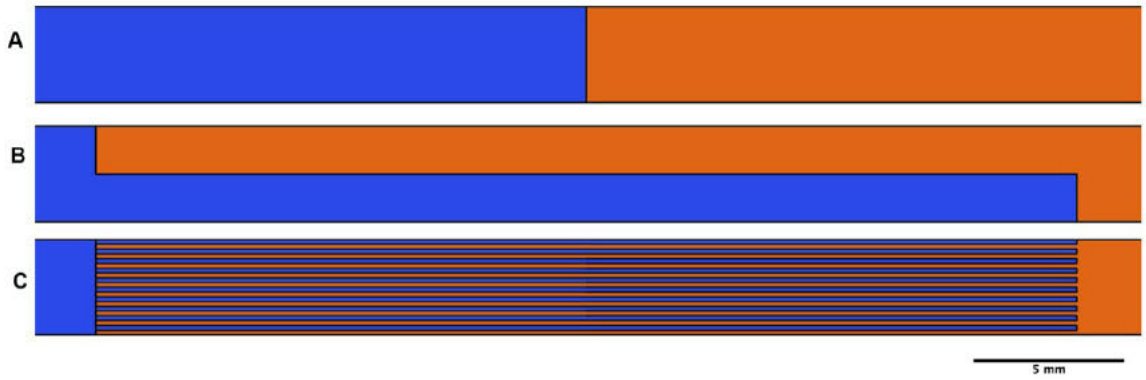

Figure 5. Diagram of the three different joints used. (A) butt. (B) lap. (C) interdigitated.

3D models were exported in STL format and sliced with Cura 5.2.1 (Ultimaker) using custom settings based on the Engineering 0.1mm profile (Table 3). Once sliced, the models were printed on either an Ultimaker S5 or S3 (Ultimaker), depending on resource availability. Regardless, two AA0.4 printcores were used as this is the smallest size nozzle (0.4mm) available for TPU printing. All samples were printed in the X-Y orientation to control for the inherent anisotropy of 3D printed parts.

*Table 3. Key settings used for the materials used in tensile testing samples. * Indicates a setting customised, otherwise Cura defaults were used.*

Setting	TPU 95A	PETG	PLA	ABS	TPLA
Layer Height (µm)	100	100	100	100	100
Line Width (µm)	400	400	400	400	400
Wall thickness (µm)	800	1200	1200	1200	1200
Wall Line count	2	3	3	3	3
Top surface skin pattern *	Concentric	Lines	Lines	Lines	Lines
Top/Bottom thickness (µm)	700	1200	1200	1200	1200
Top/Bottom layers	7	12	12	12	12
Top/Bottom Pattern *	Concentric	Lines	Lines	Lines	Lines
Connected Top/Bottom polygons *	Yes	-	-	-	-
Infill density *	50%	50%	50%	50%	50%
Infill Pattern *	Cubic Subdivision	Triangles	Triangles	Triangles	Triangles
Print speed (mm s^{-1})	25	30	30	30	30
Print cooling	Yes	Yes	Yes	Yes	Yes
Temperature (°C)	223	235	200	240	210
Build Plate Temperature (°C)	85/60	85	60	85	60

A total of five materials were used (Table 4). To model bone, four different rigid materials were used: acrylonitrile-co-butadiene-co-styrene (ABS), poly(lactic) acid (PLA), tough poly(lactic) acid (TPLA), and polyethylene terephthalate glycol-modified (PETG). To model the soft tissue of the tendon, thermoplastic poly(urethane) (TPU) was investigated.

Table 4. Chemical composition of the materials used.

Type	Manufacturer	Material (Product name)	Composition
Soft	Ultimaker	TPU 95A	Thermoplastic polyurethane
Hard	Ultimaker	PLA	Poly(lactic) acid
Hard	Ultimaker	Tough PLA	Poly(lactic) acid + acrylic polymers
Hard	Ultimaker	ABS	Acrylonitrile-co-butadiene-co-styrene, Polyethylene terephthalate, Polycarbonate
Hard	RS Pro	PETG	Polyethylene terephthalate Glycol-Modified

The infill pattern and density used were chosen arbitrarily. To examine if this had impacts on the flexibility of the TPU used, samples (*n*=1 per group) were printed in varying combinations of infill density and patterns (Figure 6).

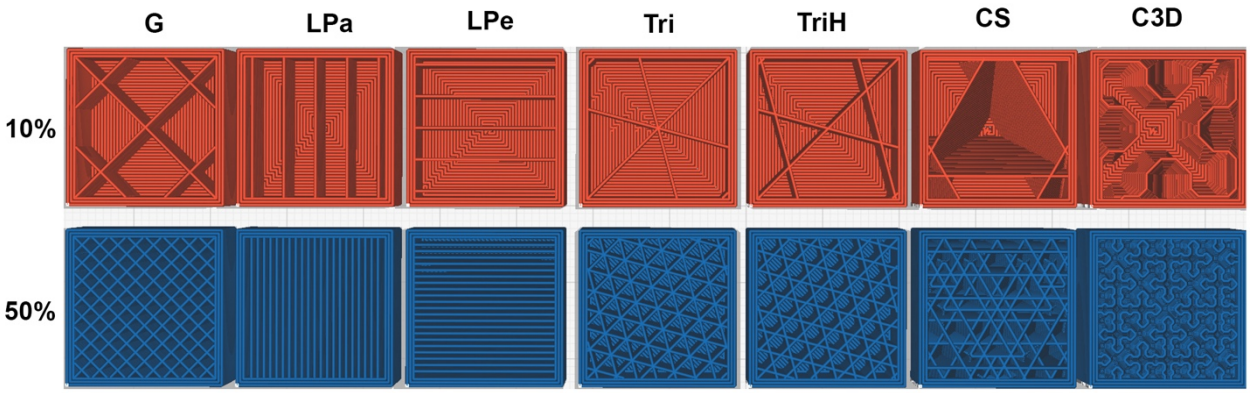

Figure 6. The effects of combining 10% (top row, red) and 50% (bottom row, blue) infill density with differing infill patterns: (left-to-right) G – grid; LPa – lines parallel to long axis; LPe – lines perpendicular to long axis; Tri – triangles; TriH – tri-hexagon; CS – cubic subdivision; C3D – cross 3D. Produced using Ultimaker Cura.

Samples were stored in a sealed container at room temperature until tensile testing to reduce moisture absorption.

Tensile testing

Samples (*n*=5 per group) were tested using a universal testing machine (Tinius Olsen H5KS) with a 5kN load cell (Figure 7). Camming grips were used in the crossheads. Samples were tested until the point of failure, as detected by the universal testing machine.

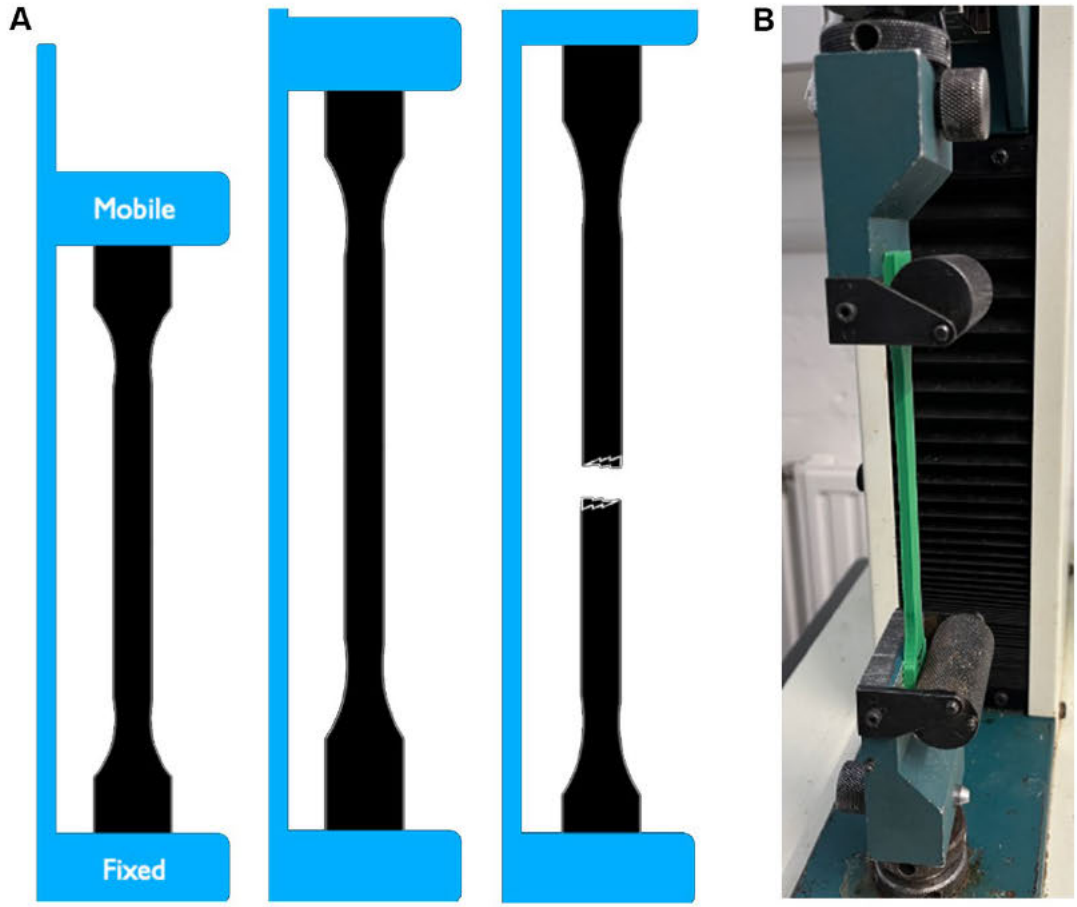

Figure 7. (A) Diagram of the universal testing machine fixed and mobile crossheads showing increasing distance between the mobile and fixed crossheads due to force applied until the point of sample failure. (B) Photograph of the apparatus used with sample loaded.

Initial testing using the protocol from the British Standards Institution (2019) revealed that the recommended speed of 1 mm min^{-1} was impractical as the time to sample failure at this speed was excessively long, especially for samples containing TPU. Further testing revealed that practical speeds of testing varied depending on the materials of the test sample (Table 5). The entirely TPU samples were tested at significantly higher speeds, as indicated in BS EN ISO 37:2017 (British Standards Institution, 2017).

Table 5. Rates of extensions used in tensile testing depending on sample type

Sample type	Rate of extension (mm min^{-1})
Solid, lap, butt	30
Interdigitated	100
TPU solid samples	250
TPU various infills	400

Stress was calculated according to the formula $\sigma = F/A$ where σ is stress in MPa, F is force applied in N, and A is the initial cross-sectional area of the sample in mm^2. Strain was calculated using the formula $\varepsilon = 100 \cdot \frac{(L_f - L_i)}{L^i}$ where ε is percentage stress, L_f is the final length of the sample, and L_i is the initial length of the sample.

Cytotoxicity assays

Due to time constraints, all cell culture work was performed by Vinothini Prabhakaran, but all analysis was undertaken independently. Incubation was performed at 37°C in a 5% CO_2 95% O_2 atmosphere at 95% relative humidity. Passage 10 primary adult differentiated rat osteoblasts (dRObs) (Cell Applications Inc.) were used in all cell culture work. Both ABS and TPLA were not evaluated for cytocompatibility due to time constraints.

Samples for cytotoxicity and cell adhesion were designed to fit into a 96-well plate in Fusion 360 (Autodesk). Samples of PETG, PLA and TPU 95A were used. A disc of each was produced, as well as bilayered discs comprised of half PETG or PLA and half TPU 95A, stacked vertically (Figure 8).

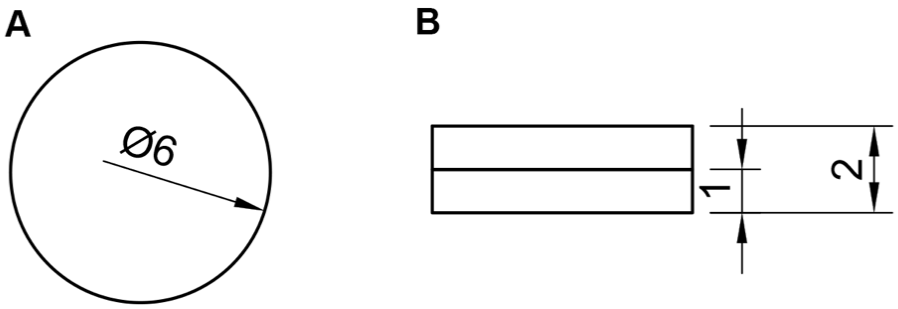

Figure 8. (A) Diameter and (B) thickness in mm of cell assay material discs

Extract media assay

Briefly, scaffold discs (experimental groups *N*=5, replicates per group *n*=2) were sterilised by immersion in 70% ethanol, and added separately to T25 flasks in 7 ml Dulbecco's Modified Eagle Medium (sDMEM) supplemented with 10% foetal bovine serum (FBS) and 1% antibiotic-antimycotic solution and incubated for 4 days. Subsequently, $1x10^5$ differentiated rat osteoblasts (dRObs) were seeded in a 24 well plate in sDMEM. After 24 hours of incubation, media was removed and replaced sDMEM from each group (n=2 per treatment group and dead control, *n*=3 for live control). After 24 hrs culture media was extracted and 70% ethanol was added to the dead control wells and incubated for 30 minutes.

Cells were washed once with phosphate-buffered saline (PBS) and 200µl of calcein-AM (2 µM) and propidium iodide (2.5 µM) were added to each well before being incubated for 30 minutes. Cell viability was assayed by calcein (excitation 475nm, emission 500-550nm) and propidium iodide (excitation 520nm, emission 580-640nm) fluorescence after 24 hrs of incubation using a GloMax Discover microplate reader (Promega). Blank control wells were used to eliminate background fluorescence and off-target fluorescence.

Direct contact assay

Direct cytotoxicity was tested by placing a drop of cell suspension (20 µl) containing $2x10^4$ cells on each scaffold disc in a 24 well plate (*n*=3 for single material discs, *n*=2 per side for bilayered discs). After 24 hours incubation, media was removed, and discs were washed once with PBS. 20µl of TrypLE Express (Gibco) was added to each disc and discs were incubated for 5 minutes. 1ml of sDMEM was added to each disc and the plate gently rocked to dislodge cells from the disc surface. Cell viability was assayed using trypan blue staining and counting cells using a haemocytometer. Live cells excluded trypan blue and were counted. The total number of live cells per ml was calculated and compared to the number of cells seeded: $\%\, Viable\ cells\ =\ 1.2(live\ cell\ counted)$ after accounting for the volume of the haemocytometer chamber, the volume of the aliquot used, and the initial number of seeded cells.

Cell adhesion assay

To ascertain the viability of these materials for use as potential tissue engineering scaffolds, it is necessary to determine how well – if at all – cells are able to adhere to the material. Preliminary testing showed that PETG discs were unsuitable for assaying cell adhesion due to the material's borderline hydrophobicity (Kováčová *et al.*, 2020; Förch *et al.*, 2009). Consequently, single material discs with the addition of a small lip to ensure the droplet of cell suspension stays on the surface of the disc were manufactured (Figure 9).

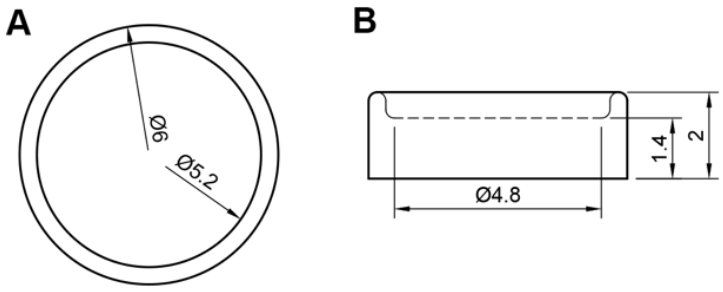

Figure 9. (A) Inner and outer circumference and (B) overall thickness, well, depth, and well circumference at base in mm of the disc with lip used for cell adhesion assays.

A dead cell control well was produced by exposing cells to 70% ethanol for 15 minutes. Media was removed and all wells were washed with PBS twice. 10µl of calcein-AM (2 µM) and propidium iodide (2.5 µM) were added before incubation for 15 minutes. Subsequently, 10µl of Hoechst 33258 (1.6 µM) was added to each well and incubated for 15 minutes. Wells were washed with PBS once more.

Images were acquired using a Zeiss AxioImager M2 upright epifluorescence microscope. Excitation and emission wavelengths were the same for calcein-AM and propidium iodide as used in the plate reader, and Hoechst 33258 was imaged at 352/461nm respectively. Each disc was placed on a glass slide before being image capture.

Raw images were processed in FIJI (Schindelin *et al.*, 2012) to remove background fluorescence via the rolling ball method with a radius of 50 pixels. The channels were split and saved before being recombined to form a merged image. Qualitative comparisons were then made between the images acquired.

Tissue engineering scaffold design

Data from Mortimer *et al.* (2021) were used to inform the design of an anatomically relevant structure for tissue engineering at the flexor digitorum profundus (FDP) enthesis in the distal phalanx (Figure 10A). The morphology of the footprint of the tendon was traced in Fusion 360 (Autodesk) and offset by 2mm before being extruded to form a 3D bone anchor. Next the outline of the FDP footprint was extruded at insertion angle of the tendon fibres (Figure 10B). This model was then exported as an STL and Ultimaker Cura 5.2.1 was used to slice the model. By using only infill a highly porous anatomically correct TPU tendon scaffold emerging from a PLA bone anchor was produced (Figure 10C). This was then printed in PLA and TPU using an Ultimaker S3 with two AA0.4 printcores.

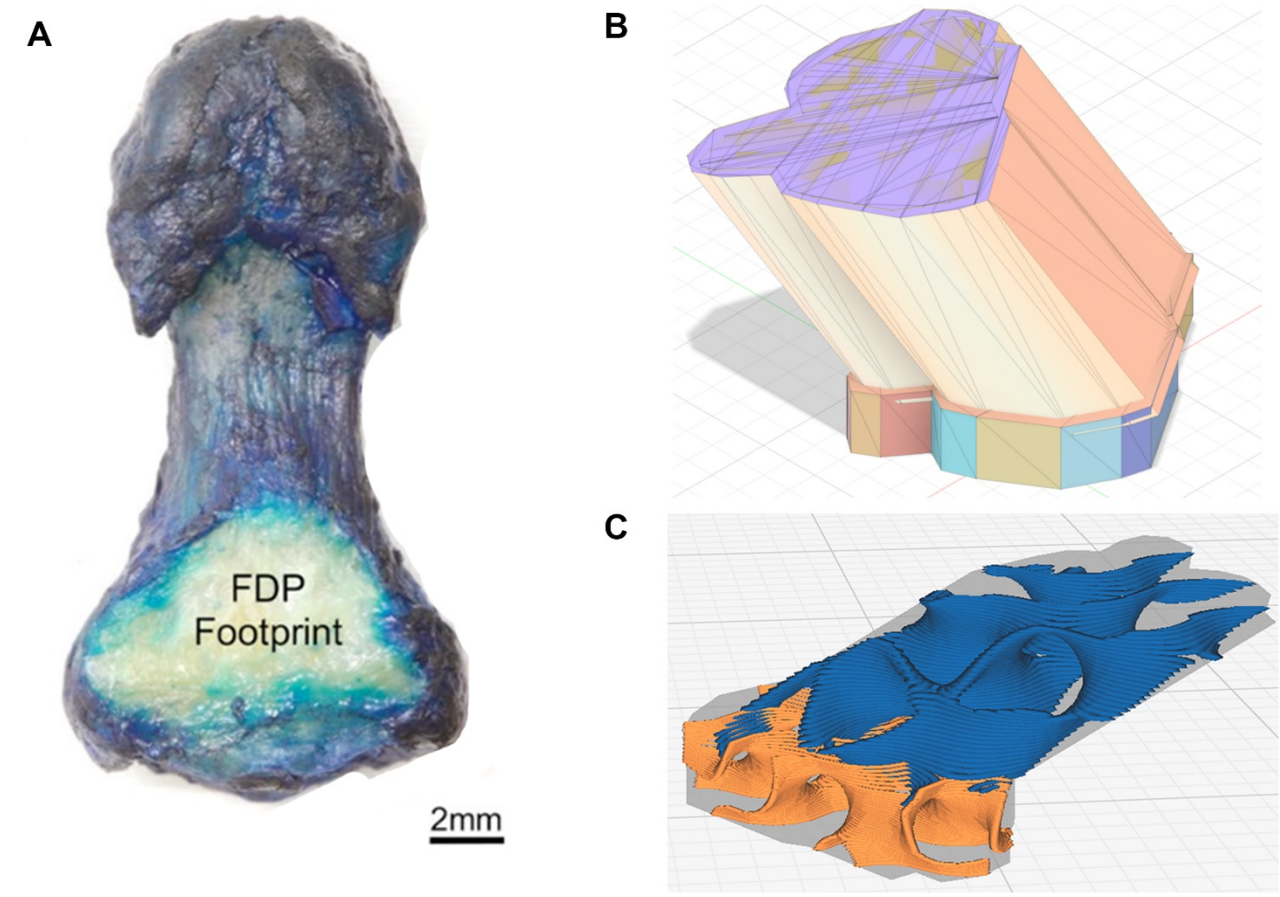

Figure 10. (A) The morphology of the footprint of the flexor digitorum profundus (FDP) tendon on the distal phalanx; reproduced from Mortimer et al. (2021). (B) The tessellated model of the FDP footprint and tendon. (C) The sliced model using only infill, increasing its porosity in a reproducible, customisable manner.

Data analysis

Tensile properties

Analysis of the raw data was performed with R v4.2.2 (R Core Team, 2022). The raw data obtained from tensile testing was used to calculate stress and strain. This process was repeated for each file of raw data per sample group. These data were combined and plotted (Wickham, 2016). The *mgcv::gam* function (Wood, 2016) was used to generate the generalised additive model (GAM) with cubic regression basis splines (Equation 1A-B).

$$\textbf{Equation 1A}: y_i = g(\mu_i)$$

$$\textbf{Equation 1B}: g(\mu_i) = f(x_i)$$

Where the response variable y_i has expectation μ_i and g is a link function (Wood, 2011).

The inbuilt optimisation functions were used to fit the model choosing the most appropriate number of knots *k*, and smoothing parameter λ with the generalised cross validation method to produce a smooth line of best-fit, with appropriate 95% confidence intervals (Figure 11).

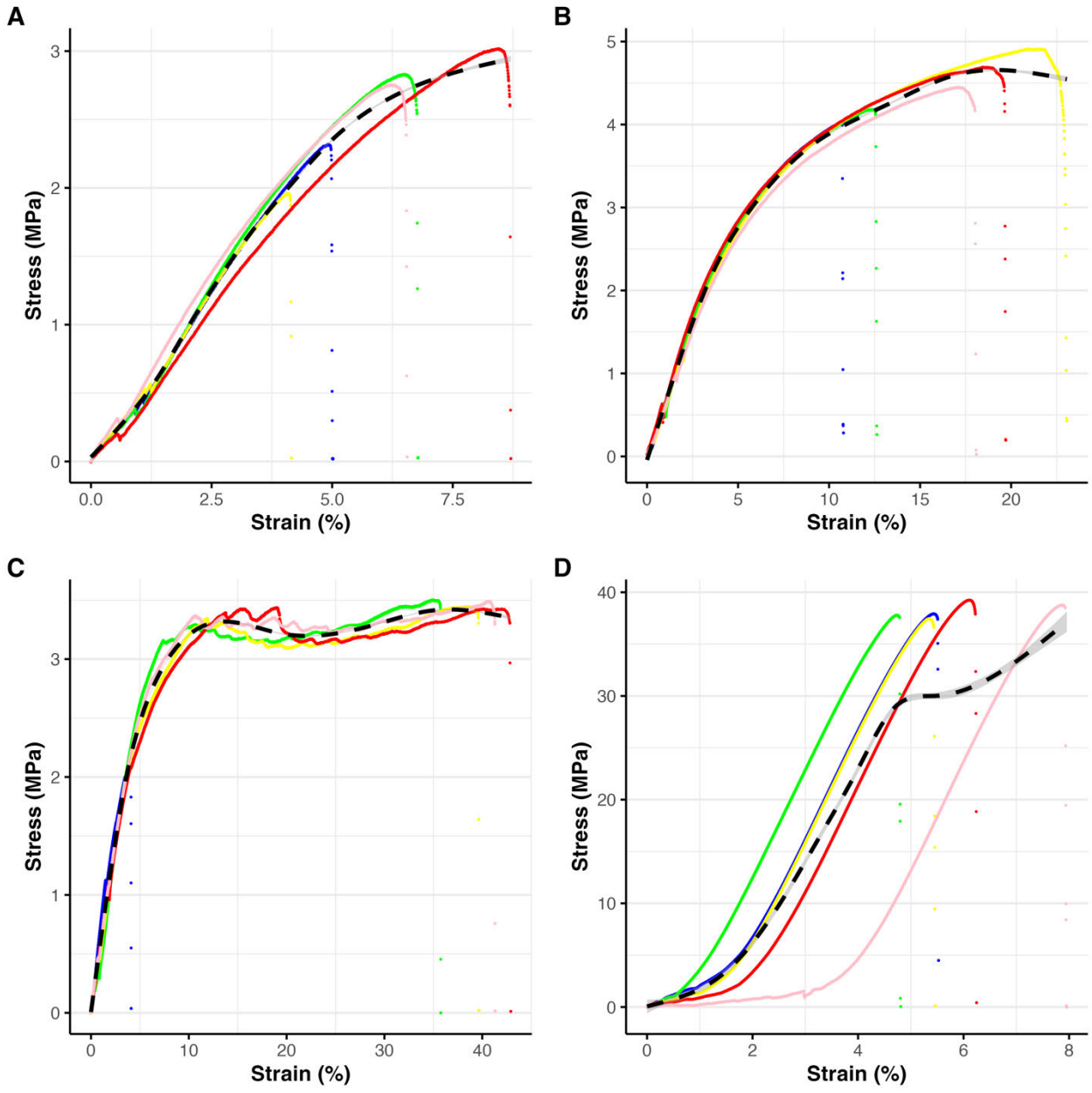

Figure 11. Stress-strain curves showing the fitted generalised additive model (dashed black line) with standard error of the mean shown (grey shaded region) compared to data points from individual samples (coloured points) for (A) ABS-TPU butt joint, (B) PLA-TPU interdigitated joint, (C) TPLA-TPU lap joint, (D) solid PETG.

The output from this model consisted of 80 points used to plot the fitted curve. A subset of these points (Table 6) were used to construct a linear model (Equation 2) through the initial elastic linear region of the stress-strain curve obeying Hooke's law.

Table 6. Initial (p_1) and final (p_2) indices of points used in plotting the linear model per joint type.

Joint type	p_1	p_2
Solid	20	30
Lap & interdigitated	1	10
Butt	30	40

Equation 2: $y = m_{lm}x + c_{lm} \text{ for } x \in [p_1, p_2]$

Young's modulus was taken to be the gradient of linear model: m_{lm} (Figure 12).

Subsequently, to find the yield point, the position of the points plotted by the fitted GAM were compared to the linear model by calculating the determinant of vectors (Equation 3).

Equation 3: $det(X_i, Y_i) = (x_2 - x_1) \cdot (Y_i - y_1) - (y_2 - y_1) \cdot (X_i - x_1)$

$$Where \quad \begin{matrix} y_1 = 0 & x_1 = \dfrac{-c_{lm}}{m_{lm}} \\ y_2 = 10 & x_2 = \dfrac{(10 - c_{lm})}{m_{lm}} \end{matrix}$$

X_i and Y_i are the values for each point and were used to determine the determinant at each point. From this, it was possible to obtain a value for how close the point lies relative to the linear model. If the absolute value of the determinant for a point – $j = (X_j, Y_j)$ – was less than d distance (Table 7) from the line (Equation 4), the point j was considered to be in the linear region (Figure 12).

Table 7. Maximum absolute distance between points generated by generative additive models and linear model in the linear region of the stresss-strain curve per joint group.

Joint type	d
Solid PLA-PLA	1.00
Solid	0.75
Lap	2.00
Butt & interdigitated	1.00

Equation 4: $|det(X_i, Y_i)| < d$

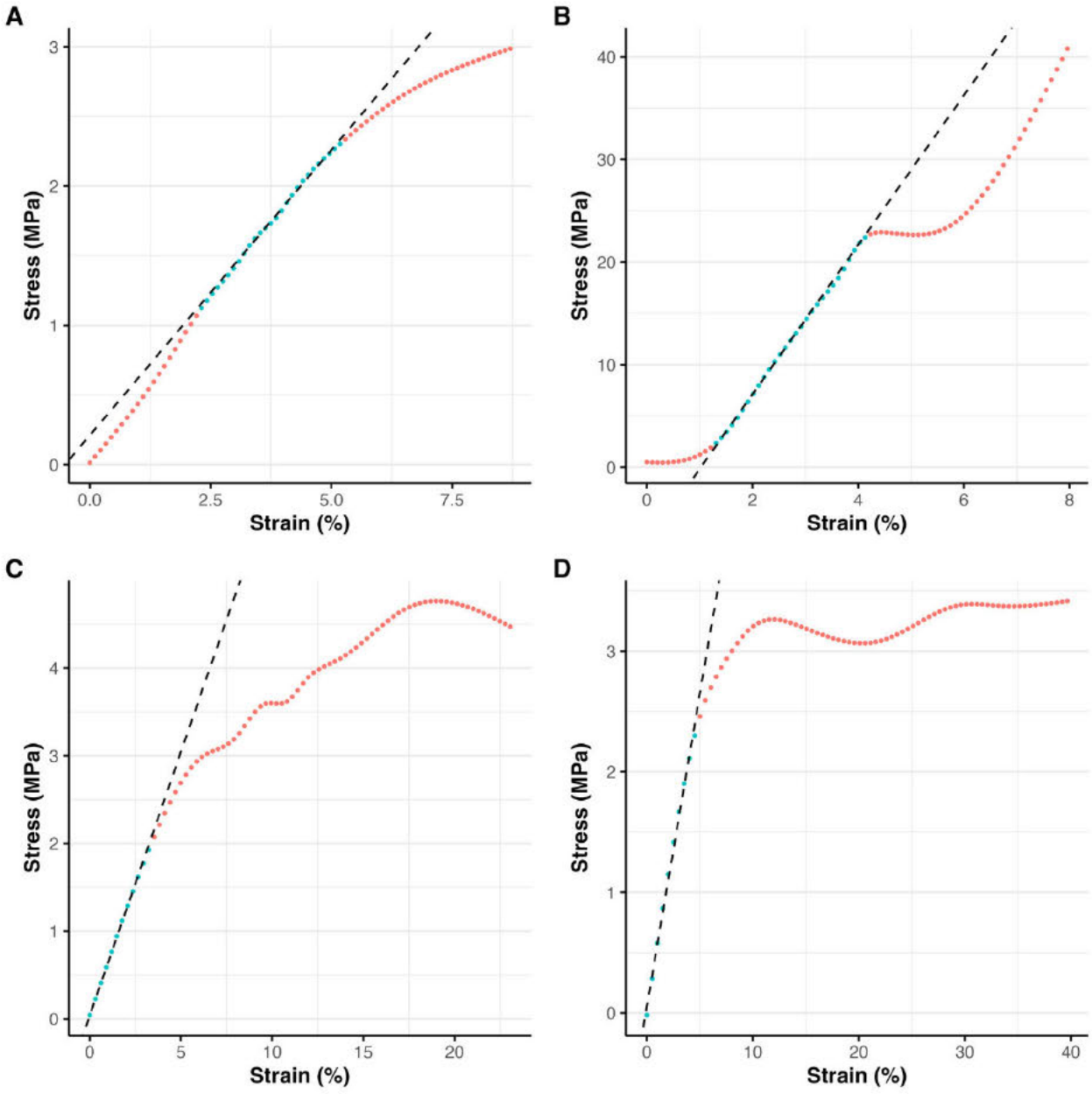

Figure 12. Linear models (dashed black line) used to find Young's modulus compared to the generalised additive model (coloured points). Points are coloured red if the distance between the point and the linear model is greater than d, and teal if the distance is less than d for (A) ABS-TPU butt joint, (B) PLA-TPU interdigitated joint, (C) TPLA-TPU lap joint, (D) solid PETG.

The maximum value of the longest uninterrupted sequence of points found to be in the linear region by this method was taken to be the yield point.

Table 8. Summary of how each key value was determined.

Value	Calculation method
Ultimate stress	Maximum stress value in GAM
Stress at fracture	The stress value of the final point in GAM
Stress at yield	The stress value of the yield point in GAM
Young's modulus	Gradient of the linear model fitted to GAM

Finally, this information was combined to produce stress-strain curves and determine key tensile properties of each material and joint combination (Figure 13).

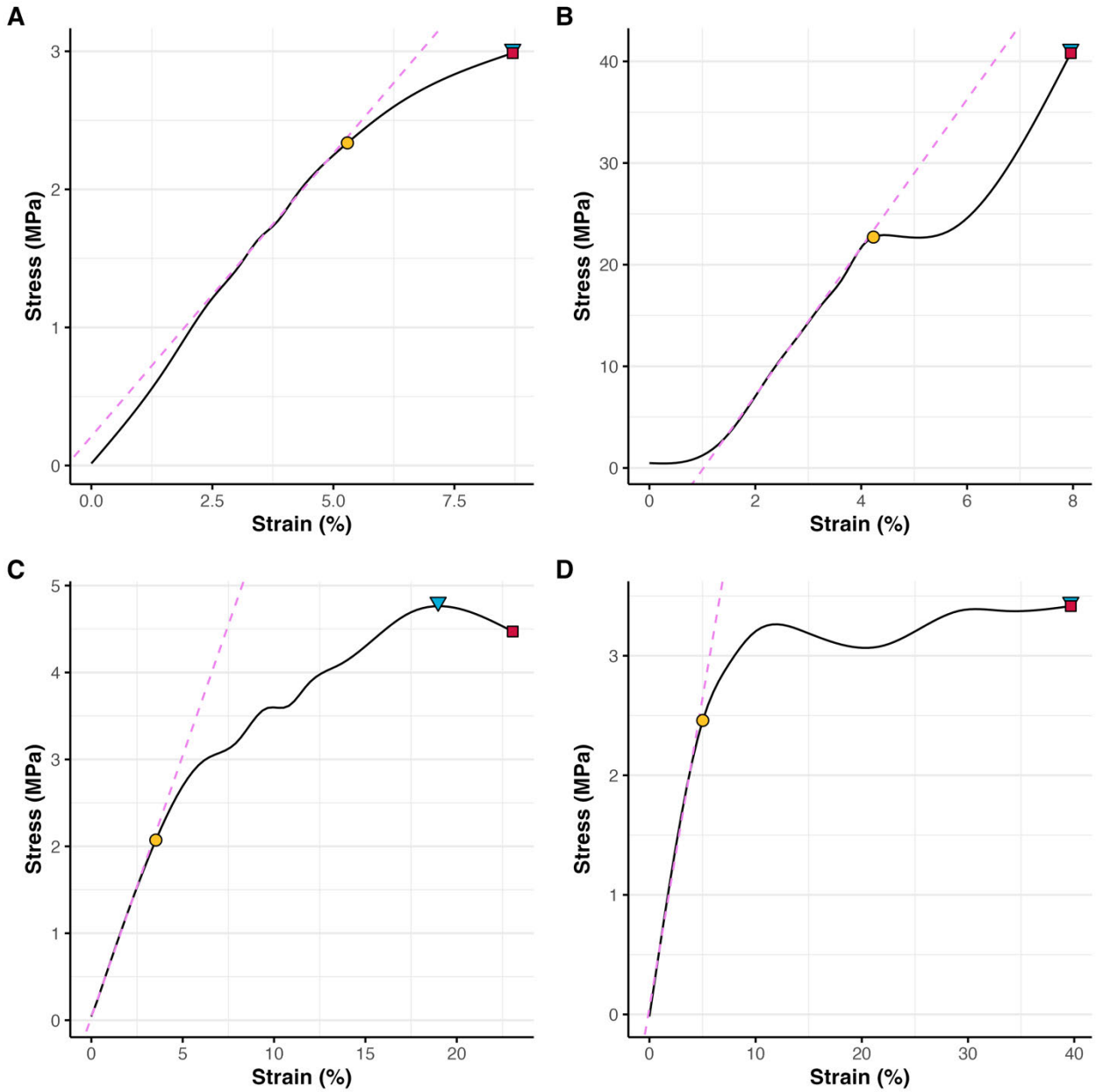

Figure 13. Tensile strength at break (red square), ultimate tensile strength (blue triangle), and yield point (yellow circle) shown compared with linear models used to calculate Young's modulus (dashed pink line) and generalised additive model curves for (A) ABS-TPU butt joint, (B) PLA-TPU interdigitated joint, (C) TPLA-TPU lap joint, (D) solid PETG.

Statistical methods

Results were analysed using R v4.2.2 (R Core Team, 2022). For all statistical tests, α was set at 0.05, with $P \leq 0.05$ being regarded as statistically significant.

Cytotoxicity assays

One-way analysis of variance (ANOVA) followed by Tukey's HSD multiple comparisons *post-hoc* test was used to examine differences between multiple groups.

Statistical power was analysed *a priori* using G*Power (Faul *et al.*, 2007). Given an expected effect size f = 0.25 with α set at 0.05, and β set at 0.20 a total sample size needed would be 200 (40 per experimental group) for a power of 0.80. This was seen as logistically unfeasible. Consequently, the actual power for indirect cytotoxicity testing was 0.065, and for direct cytotoxicity testing it was approximately 0.077.

Tensile testing

Mean strain at failure, mean ultimate strain, and mean strain at yield were analysed individually. To ensure a robust analysis using two-factor analysis of variance (ANOVA) with type III sums of squares, four linear models were fitted through the data and subsequently analysed for goodness of fit. Weighted least-squares regression was used in some models with weightings determined iteratively. Otherwise, ordinary least squares regression was used. Orthogonal contrasts were also employed for both factors.

To evaluate the fit of the models the Rainbow test for normality, the Breusch-Pagan test for heteroscedascity, the Shapiro-Wilk test for normality of the residuals of the model, and the residual standard error, and adjusted R^2 were used.

Two-factor ANOVA was followed by Tukey's HSD *post-hoc* test to provide multiple comparisons. The sample size of 5 per group was chosen in line with (British Standards Institution, 2012) and therefore no power analysis was conducted.

Results

Multi-material 3D printing

After careful optimisation of print parameters and part orientation, it was demonstrated that all material combinations used in this study were feasible to print (Figure 14).

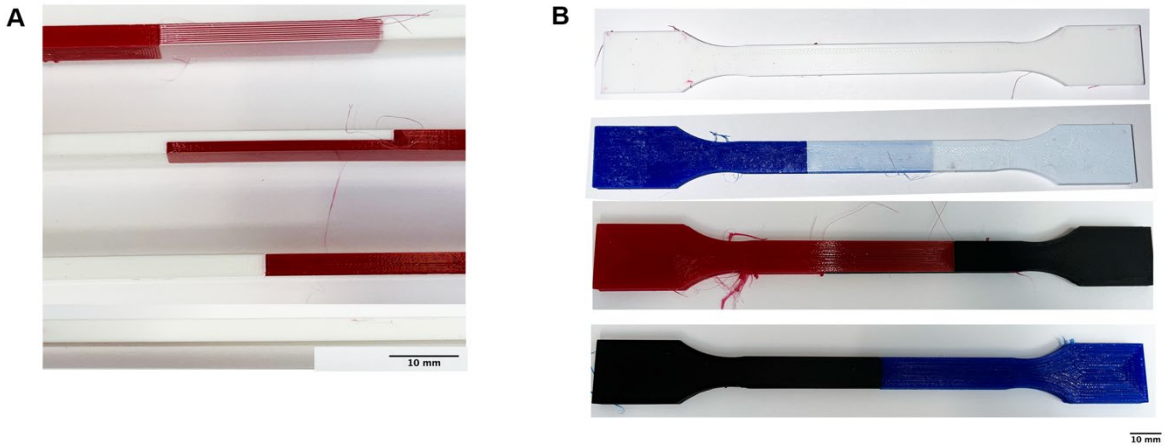

Figure 14. (A) Side profiles of successfully printed (top to bottom) interdigitated, lap, butt and solid samples. (B) Front profiles of (top to bottom) solid, interdigitated, lap, and butt joints printed in a variety of materials.

Tensile testing

Linear model fitting

Before assessing the four model types employed, evaluation of the optimum linear model of the tensile data recorded converged on a model with the weighting term $Stress/_{100}$. Subsequently, the four models were evaluated using various statistical tests to ensure the assumptions of a two-factor ANOVA were met. Namely, heteroscedascity and normality. Linearity of the data was also evaluated, as violation of this assumption would invalidate the use of a linear model. Finally, these results lead to the use of a weighted model with an interaction term for the effects of joint type and material combination (Table 9).

Table 9. Comparisons of linear models fitted through tensile stress data. To evaluate the fit of the models the Rainbow test for normality, the Breusch-Pagan test for heteroscedascity, the Shapiro-Wilk test for normality of the residuals of the model, and the residual standard error, and adjusted R^2 were used.

Model	Rainbow test		Breusch-Pagan test (Studentised)		Shapiro-Wilk test		Model fit			
	$Rain_{(df1, df2)}$	*p*	$BP_{(df)}$	*p*	W	*p*	Adjusted R^2	Residual Standard $Error_{(df)}$	$F_{(df, df)}$	*p*
Weighted & interaction	$0.58_{(1, 17)}$	0.90	$0.40_{(11)}$	1	0.95	0.026	0.966	$0.051_{(46)}$	$148.5_{(11, 46)}$	$< 2.2x10^{-16}$
Weighted & no interaction,	$2.1_{(29, 23)}$	0.039	$0.62_{(5)}$	0.99	0.98	0.30	0.935	$0.070_{(52)}$	$166_{(5, 52)}$	$< 2.2x10^{-16}$
Unweighted & interaction	$0.58_{(29, 17)}$	0.90	$27_{(11)}$	0.0044	0.97	0.24	0.963	$0.32_{(46)}$	$134.8_{(11, 46)}$	$< 2.2x10^{-16}$
Unweighted & no interaction	$2.1_{(29, 23)}$	0.039	$11_{(5)}$	0.050	0.98	0.60	0.940	$0.40_{(52)}$	$180.3_{(5, 52)}$	$< 2.2x10^{-16}$

The majority of butt and lap joint samples failed with the joint separating along the rigid-compliant interface (Figure 15A). The interdigitated joints tended to fail with the compliant material pulling out of the joint, leaving behind the interdigitated layers. However, the solid samples failed around the radius of the transition between the broad and narrow sections (Figure 15B). Meanwhile, the purely TPU samples achieved very large extension, with some even failing to break before reaching the upper vertical limit of the tensile testing machine (Figure 15C). The PETG-TPU lap jointed samples had such a strong bond that the thin PETG section failed before the joint (Figure 15D).

Figure 15. Modes of failure of different sample types. (A) lap PLA-TPU; (B) interdigitated TPLA-TPU; (C) solid TPU; (D) lap PETG-TPU.

For each material and joint combination stress at yield, fracture, and ultimate stress were calculated along with their corresponding strain values. The gradient of linear elastic region of the stress-strain curve was used to calculate Young's modulus. As expected, all joints were much weaker than solid samples of the rigid materials used (Table 10).

Table 10. Mean stress and strain values for all materials except solid TPU95A.

Joint type	Material	Stress at yield (SD) (MPa)	Strain at yield (%)	Stress at fracture (SD) (MPa)	Strain at fracture (%)	Ultimate stress (SD) (MPa)	Strain at ultimate stress (%)	Young's modulus (MPa)
Butt	ABS-TPU	2.34 (0.018)	5.29	2.99 (0.046)	8.70	2.99 (0.036)	8.70	0.41
	PETG-TPU	1.78 (0.014)	3.90	2.31 (0.048)	6.85	2.37 (0.016)	6.07	0.49
	PLA-TPU	1.27 (0.012)	2.83	1.79 (0.026)	3.79	1.79 (0.026)	3.79	0.44
	TPLA-TPU	1.53 (0.014)	3.27	1.78 (0.026)	4.10	1.78 (0.026)	4.10	0.49
Interdigitated	ABS-TPU	2.76 (0.035)	4.75	6.14 (0.088)	41.59	6.14 (0.088)	41.59	0.57
	PETG-TPU	2.81 (0.043)	4.67	6.11 (0.103)	40.83	6.25 (0.046)	35.15	0.60
	PLA-TPU	2.07 (0.049)	3.53	4.47 (0.097)	23.06	4.76 (0.051)	18.98	0.59
	TPLA-TPU	2.09 (0.035)	2.96	1.19 (0.100)	77.50	3.92 (0.033)	8.84	0.45
Lap	ABS-TPU	2.79 (0.019)	4.83	3.98 (0.063)	42.37	3.98 (0.063)	42.37	0.60
	PETG-TPU	1.48 (0.016)	2.32	3.72 (0.044)	61.17	3.92 (0.019)	51.88	0.47
	PLA-TPU	2.16 (0.019)	4.52	3.24 (0.045)	35.69	3.35 (0.018)	14.45	0.51
	TPLA-TPU	2.46 (0.017)	5.02	3.42 (0.042)	39.67	3.42 (0.042)	39.67	0.52
Solid	ABS	8.75 (0.162)	1.68	25.65 (0.429)	4.16	28.00 (0.174)	3.69	7.54
	PETG	22.71 (0.265)	4.23	40.81 (0.646)	7.96	40.81 (0.646)	7.96	7.29
	PLA	16.55 (0.895)	2.53	43.49 (1.934)	6.87	43.49 (1.934)	6.87	11.71
	TPLA	12.15 (0.245)	1.72	29.65 (0.579)	3.98	33.12 (0.245)	3.53	8.83

Analysis of the effects of joint type and material combination

Omnibus two-factor ANOVA ($F_{(6, 46)} = 8.8286$, $p = 2.05\text{x}10^{-6}$) with orthogonal contrasts were used for both material and joint type was used to examine the differences between joint type, material, and the interaction between these factors. A clear effect of this interaction was revealed, in keeping with qualitative observations made during the printing process, and the tensile testing (Figure 16).

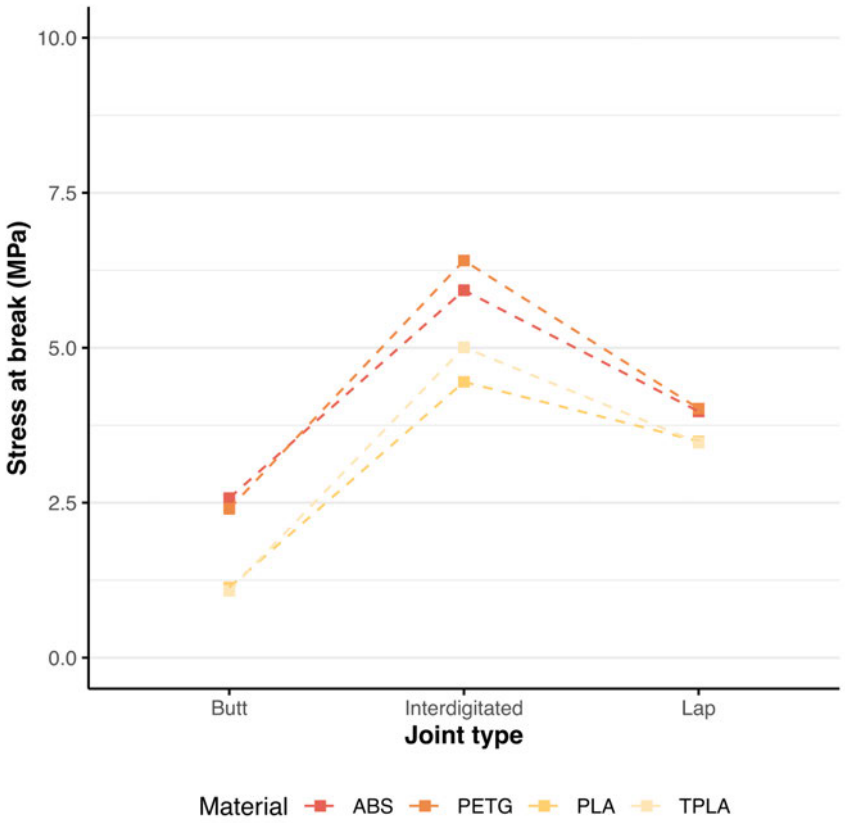

Figure 16. Interaction plot demonstrating a interactions between joint type and materials used.

Two-factor ANOVA also revealed strong evidence of differences between both the materials ($F_{(3,46)} = 53.0616$, $p = 5.65\text{x}10^{-15}$) used and joint types ($F_{(2,46)} = 621.8640$, $p < 2.2\text{x}10^{-16}$). Although some of this evidence may be misleading due to the aforementioned interaction, the magnitude of their respective F statistics suggests that joint type has a much larger effect on tensile stress at break than material. This is supported by a variety of measures of effect size (Table 11).

Table 11. ANOVA table for the omnibus two-factor ANOVA employed to examine differences between joint type, material, and their interaction alongside measures of effect size. Effect sizes reported include partial eta-squared (η_p^2), partial omega-squared (ω_p^2), and Cohen's f as well as the ANOVA F-statistic.

	ANOVA table					Effect sizes		
	Sum of squares	**Mean squares**	***df***	***F*-statistic**	***p***	η_p^2	ω_p^2	**Cohen's *f***
Joint	3.222	1.611	2	621	$< 2.2 \times 10^{-16}$	0.96	0.96	5.20
Material	0.412	0.137	3	53.1	5.65×10^{-15}	0.78	0.73	1.86
Interaction	0.137	0.023	6	8.83	2.05×10^{-6}	0.54	0.45	1.07
Residuals	0.119	0.003	46	-	-	-	-	-

Tukey's HSD *post-hoc* test was used to evaluate the differences observed within both joint type and materials (Figure 17). There was little difference seen between ABS and PETG, and between PLA and TPLA. However, large differences were seen between ABS or PETG and PLA or TPLA. The strongest joint was interdigitated, and the weakest butt.

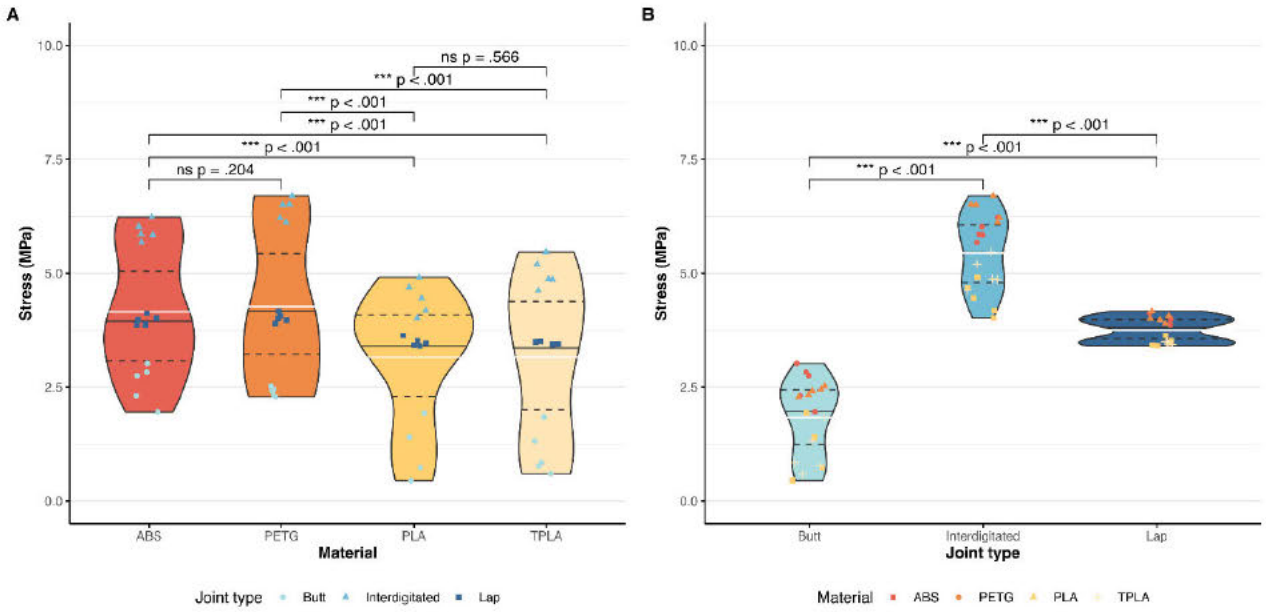

Figure 17. The effects of (A) material or (B) joint type on tensile stress at break. Dashed lines show the 25% and 75% quartiles, solid black and white lines the median and mean, respectively. Points overplotted show individual values.

To evaluate the effect of joint type on tensile stress at break for each material, Tukey's HSD *post-hoc* test was used again, averaging the results over the levels of material (Figure 18). Here, the interaction between joint type and material is clear; whilst the pattern of joint strength is maintained for each material (Figure 18B-E), there are large differences in the strength of each joint type due to the differing materials used.

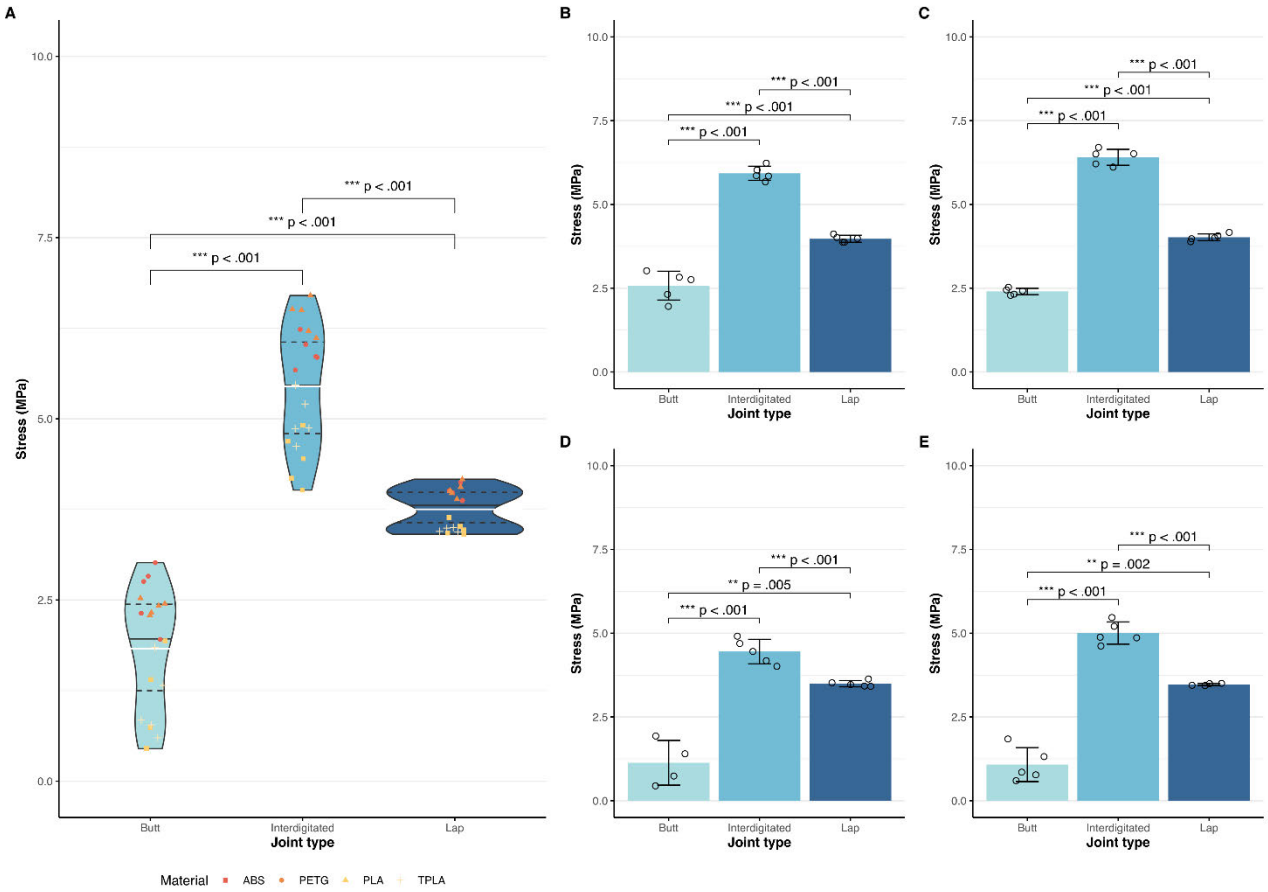

Figure 18. The effects of joint type on the tensile strength of each material. (A) Tensile testing demonstrated substantial differences in strength between the three joint types used, regardless of material combination. Dashed lines show the 25% and 75% quartiles, solid black and white lines the median and mean, respectively (reprinted from Figure X). Within each material combination, there were also large differences in the stress withstood by samples before break with 95% confidence intervals shown: (B) ABS-TPU; (C) PETG-TPU; (D) PLA-TPU; (E) TPLA-TPU.

Alongside this, Tukey's HSD *post-hoc* test averaged over the levels of joint type demonstrated a similar pattern, with interdigitated joints having the highest tensile strength, and butt joints the weakest. Unlike both butt and lap joints interdigitated joints demonstrated significant variability in their tensile strength at break depending on the material combination employed (Figure 19). This is likely due to the significant interaction found in the two-factor ANOVA reported previously.

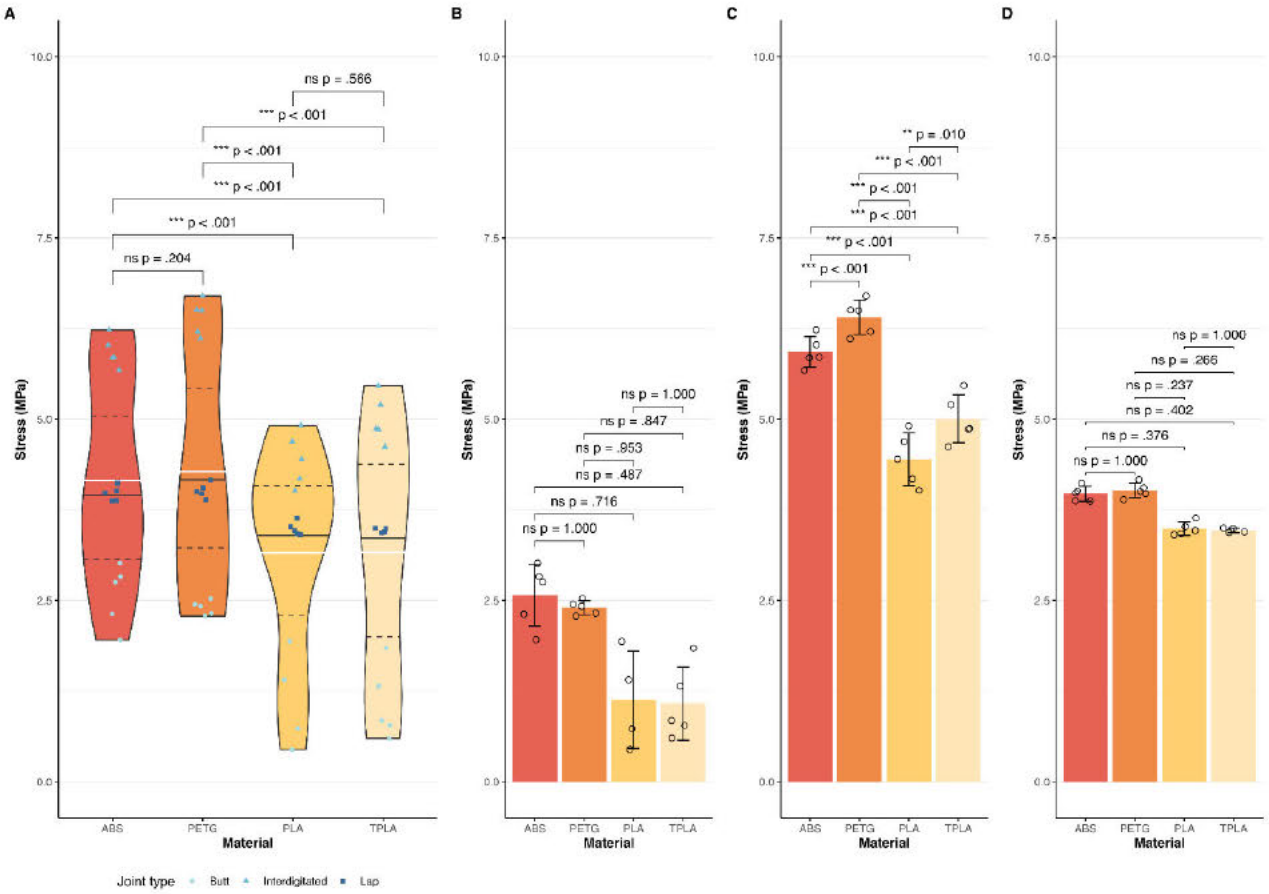

Figure 19. The effects of material on the tensile strength of each joint type. (A) Tensile testing demonstrated substantial differences in strength between the four material combinations used, regardless of joint type. Dashed lines show the 25% and 75% quartiles, solid black and white lines the median and mean, respectively (reprinted from Figure X). Within joint type, there were also large differences in the stress withstood by samples before break with 95% confidence intervals shown: (B) butt joint; (C) interdigitated joint; (D) lap joint.

Mechanical properties of elastomeric materials

As TPU 95A is an elastomeric material, there is no clear yield point as the material only undergoes elastic deformation until fracture. Consequently, the ultimate stress and strain are the same as the values for fracture. It is more useful in these materials to report the stress at X% strain (Table 12).

Table 12. Mean stress and strain values for solid TPU 95A samples.

Stress at 100% strain (SD) (MPa)	Stress at 200% strain (SD) (MPa)	Stress at fracture (SD) (MPa)	Strain at fracture (%)
5.97 (0.038)	8.92 (0.034)	12.08 (0.810)	311.51

As the infill pattern and density used for TPU 95A in multi-material samples was chosen arbitrarily, the effects these factors have on the tensile properties were compared using single-material samples (Table 13).

Table 13. Stress at 100% and 200% strain, and stress and strain at fracture for TPU95A printed in different infill densities and patterns (n=1 per density and pattern).

Stress at 100% strain (MPa)	Stress at 200% strain (MPa)	Stress at fracture (MPa)	Strain at fracture (%)	Infill density and pattern
5.73	8.51	12.99	304.26	10% Tri-hexagon
5.75	8.76	13.82	311.44	10% Cross 3D
6.04	8.845	12.255	299.815	50% Cross 3D
5.53	8.01	10.81	292.45	10% Triangle
6.90	9.76	10.51	224.22	10% Lines parallel to long axis
5.51	7.91	9.19	245.87	50% Lines perpendicular to long axis
7.32	10.06	11.30	239.65	50% Tri-hexagon

The effects of infill pattern and density were found to be so significant that five samples did not fracture at the maximum height the universal testing machine could reach (Table 14).

Table 14. Stress at 100% and 200% strain and maximum stress for TPU95A printed in different infill densities and patterns (n=1 per density and pattern) that did not fracture as it reached the vertical limit of the universal testing machine.

Stress at 100% strain (MPa)	Stress at 200% strain (MPa)	Maximum stress (MPa)	Infill density and pattern
7.29	10.70	14.71	50% Cubic subdivison
5.78	8.48	13.34	50% Grid
6.71	8.57	14.20	50% Lines parallel to long axis
6.63	9.54	13.87	50% Triangle
7.87	11.51	17.68	10% Grid

Tissue engineering scaffold production

The model of the FDP insertion was optimised over ten iterations to obtain a balance between structural integrity and maximum porosity. Ultimately, 10% gyroid infill for the TPU and 14% gyroid for the PLA were found to produce repeatable prints. Additionally, both bed adhesion in the form of a PLA raft and tree supports were found to be necessary and simple to remove to enable the model to print. Combined, these settings enabled the printing of an anatomically accurate highly porous scaffold with excellent adhesion between rigid and compliant materials (Figure 20).

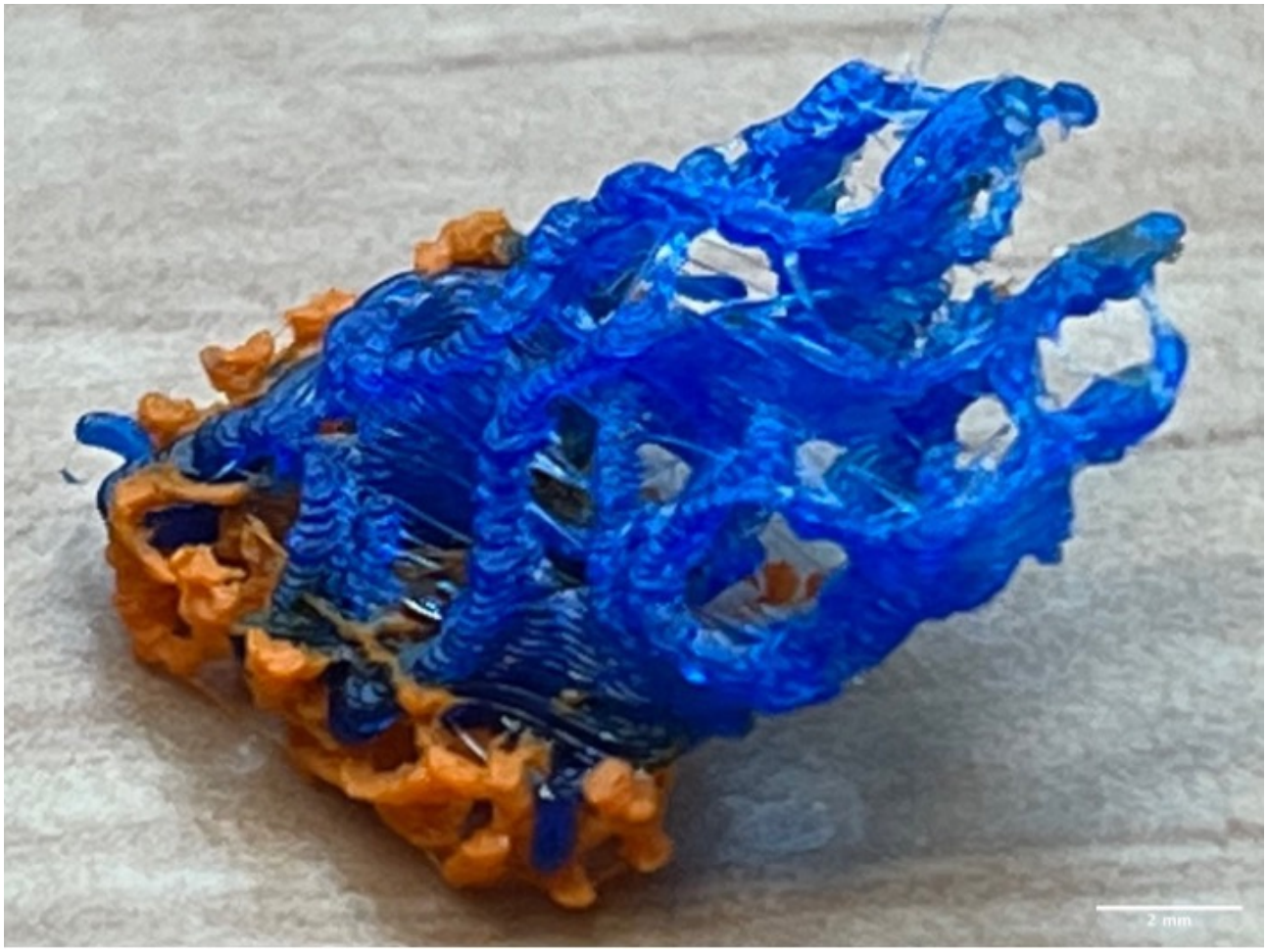

Figure 20. The final FDP scaffold showing the interface between the rigid PLA bone anchor (orange) and the compliant TPU tendon scaffold (blue).

Indirect cytotoxicity

Indirect cytotoxicity testing revealed little difference between materials: all materials analysed were deemed non-cytotoxic to differentiated rat osteoblasts (dRObs).

Calcein-AM fluorescence (Figure 21A) (as a percentage of control) was greatly reduced in the dead control compared with the live control. Conversely, little difference was observed between the live control and the various material groups. This demonstrates the presence of active intracellular esterases (Uggeri *et al.*, 2000) and therefore live cells in all material groups in comparable numbers to the live control.

Likewise, for propidium iodide (PI) fluorescence (Figure 21B), the live and dead controls were different. Whereas there was little difference between the material groups and the live control. This indicates that cell membranes were intact in all groups except the dead control as PI must bind to DNA to fluoresce but cannot traverse an intact cell membrane (Crowley *et al.*, 2016); hence, PI is used as a marker of cell death.

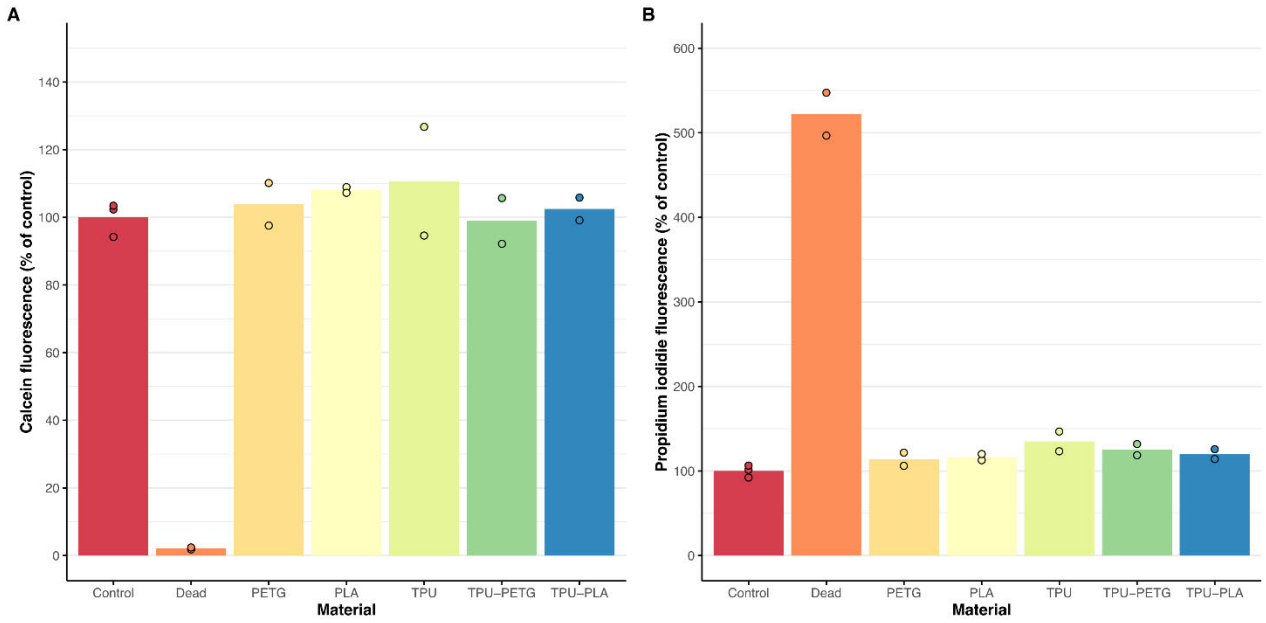

Figure 21. (A) Calcein-AM fluorescence demonstrated there was little difference in cell viability between dROb cell growth in media exposed to the materials for 5 days. (B) Propidium iodide fluorescence demonstrated there was little difference in cell death between dROb cell growth in media exposed to the materials for 5 days. Results are presented as the mean fluorescence reading with the live control set as 100%, and data points overlaid.

Qualitatively, there appeared to be few visual differences between dRObs grown in standard sDMEM (Figure 22A), and those grown in media incubated with the material discs for five days (Figure 22C-G). However, the dead control (Figure 22B) was noticeably different (lack of colour is due to removal of growth media containing phenol red). Quantitative image analysis was deemed unfeasible as cells are not monolayered, and therefore image analysis would be complex and likely inaccurate.

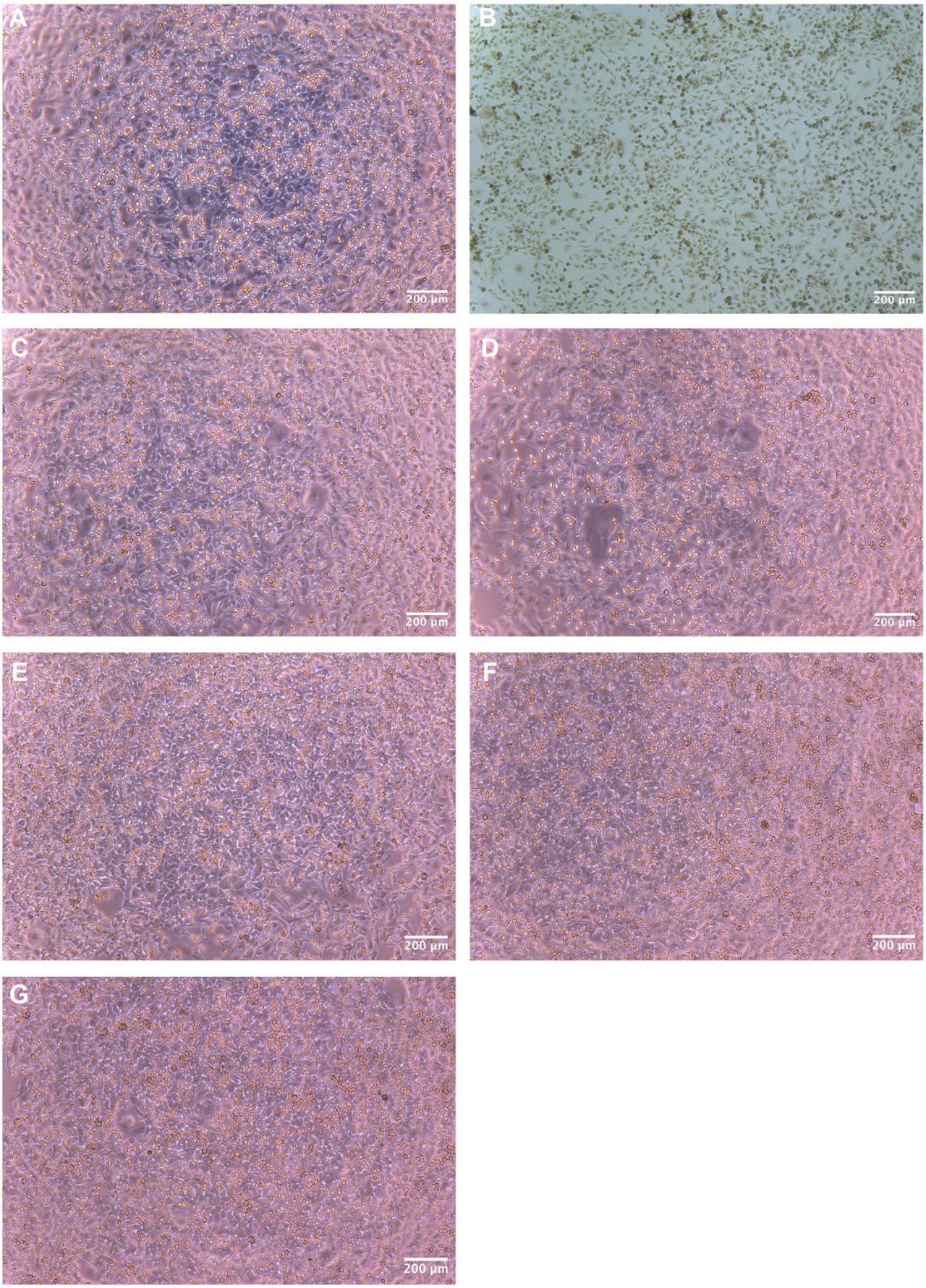

Figure 22. Representative photomicrographs of differentiated rat osteoblasts (dRObs) growing in media exposed to (A) control, (B) dead control, (C) PLA, (D) PETG, (E) TPU, (F) TPU-PETG, (G) TPU-PLA. Scale bar 200 µm.

Direct cytotoxicity

Assessment of cell viability, as assayed by trypan blue exclusion (Figure 23), was limited the extent to which these data could be interpreted the small sample size (7 groups, and 17 values); as well as the lack of a control count due to an oversight in the experimental design. Consequently, formal statistical testing was not undertaken as the results were likely to be misleading and assumptions of the tests violated, especially considering the extremely wide range of the data. However, these data did show that all material combinations had at least a small number of viable cells in at least one replicate.

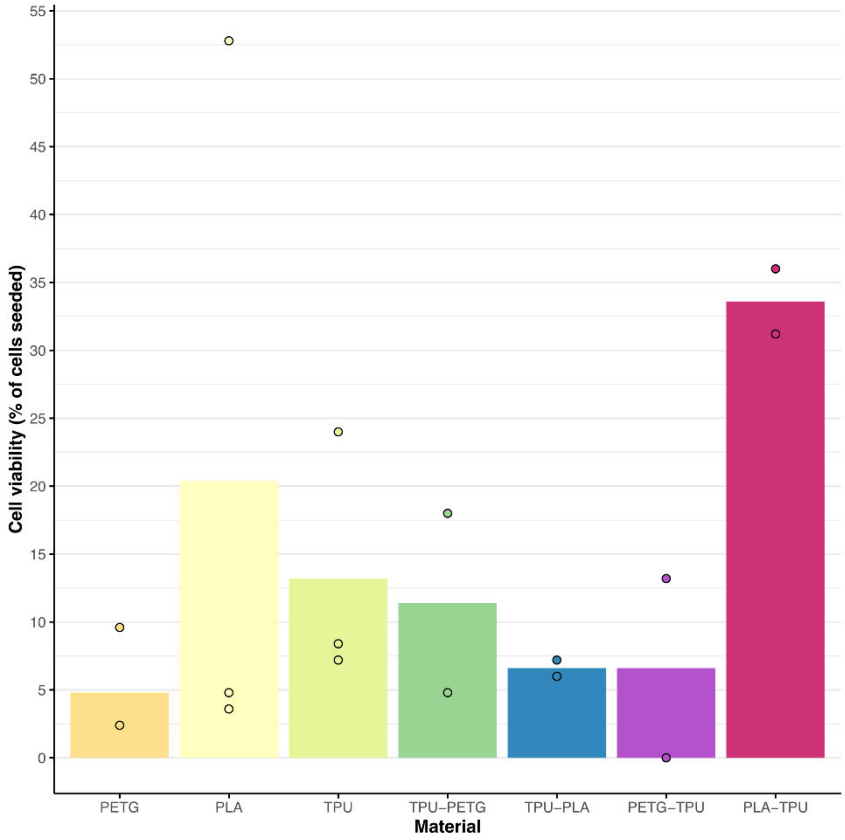

Figure 23. Percentage of viable cells found through trypan blue exclusion per material group. Results are presented as the mean percentage cell viability with the number of cells seeded ($2x10^4$) set as 100%, and data points overlaid.

Cell adhesion

Cell adhesion was initially examined on the same discs used in the direct cytotoxicity assays. However, phase-contrast microscopy revealed the droplet of cell suspension had rolled off of the PETG discs and adhered to the substrate below (Figure 24). Moreover, due to the opaque nature of the discs used, cells were unable to be visualised on the discs' surface.

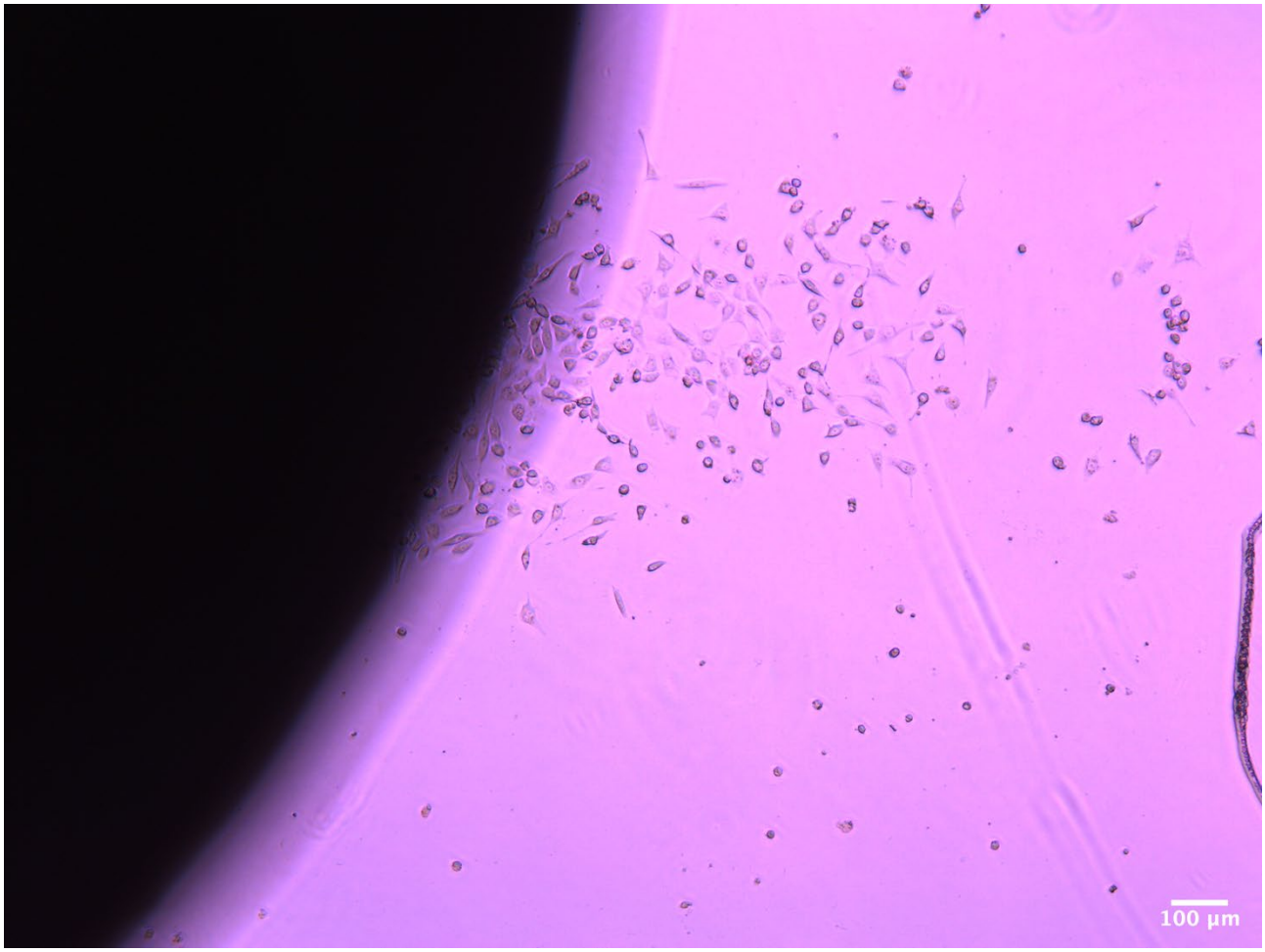

Figure 24. PETG discs (black circle, left) were found to be unsuitable for direct cell contact assays as the cell suspension would roll off of the disc leading to dRObs adhering to the substrate below, as seen here.

Consequently, new discs were designed with a well to hold the cell suspension in position. Epi-fluorescence microscopy illuminated the cell adhesive and non-cytotoxic properties of PETG, PLA, and TPU (Figure 25). Once again, the multi-layered growth of dRObs on these substrates prohibited quantitative analysis.

Calcein-AM fluorescence demonstrated numerous healthy dRObs on all materials (Figure 25A-C). Propdium iodide revealed low numbers of dead cells on PETG and PLA (Figure 25E-F) but stronger staining was seen on TPU (Figure 25D). Hoescht 33258 fluorescence showed many nuclei on TPU and PLA (Figure 25G, I) but a conspicuous absence of fluorescence on PETG (Figure 25H).

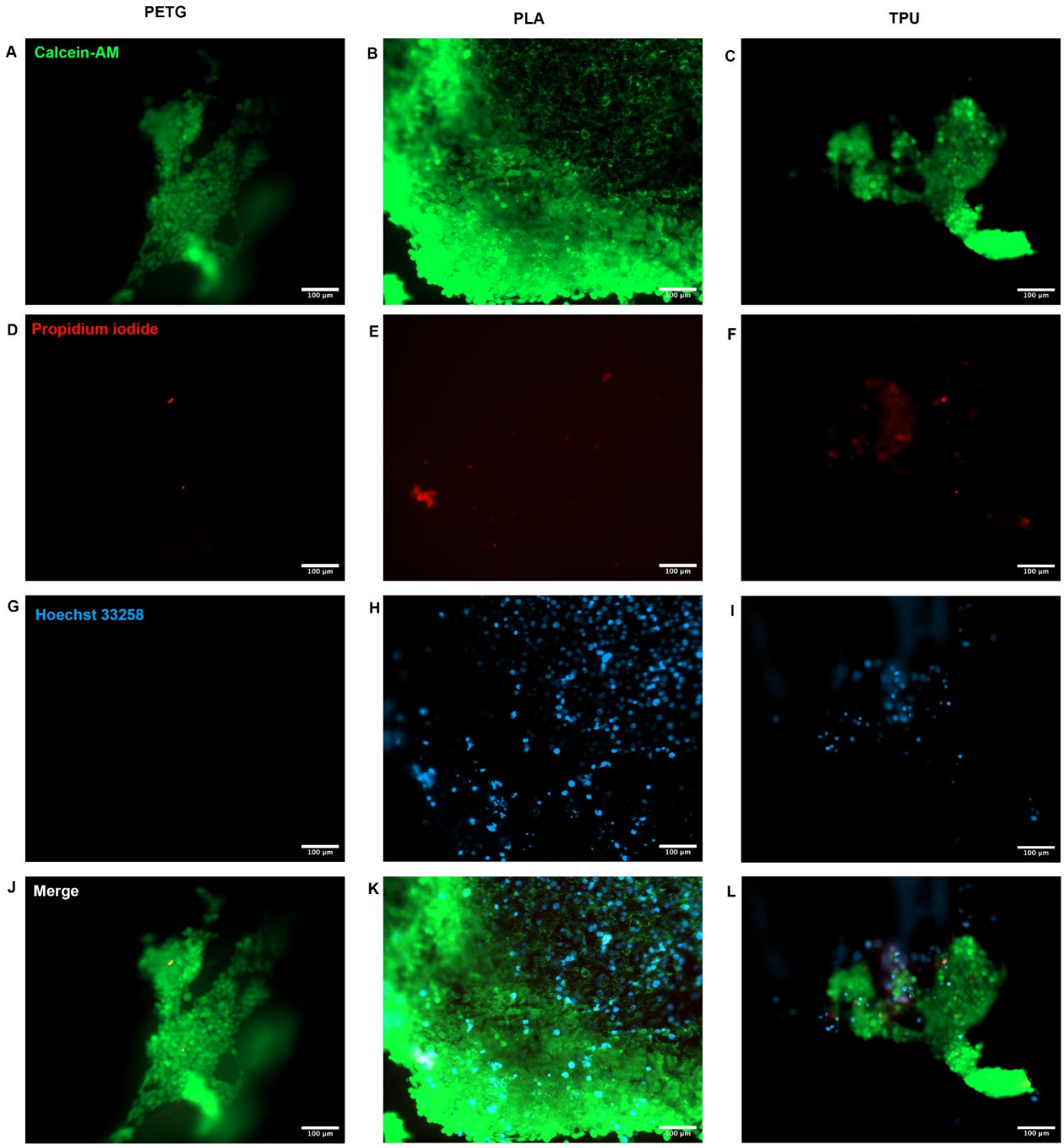

Figure 25. Representative epifluoresence photomicrographs of (A, D, G, J) PETG; (B, E, H, K) PETG; (C, F, I, L) TPU showing single channels for (A-C) calcein-AM; (B-F) propidium iodide; (G-I) Hoechst 33258; (J-L) merge of all three channels. Scale bars 100 µm.

Discussion

The twin aspects of this project will be discussed sequentially. Firstly, I aimed to 3D print two materials cohesively and characterise the tensile properties of the composites produced. Secondly, I examined the cytotoxicity, and cell adhesion of these materials using dRObs.

Tensile testing

Tensile testing revealed that there were large differences between joint types, and between ABS and PETG versus PLA and TPLA (Figure 17). Within these two groups of material combinations the differences were more subtle, and often did not reach statistical significance (Figure 19A). This is understandable given the inherent differences between these two groups.

The strength of the joints followed the pattern expected: tensile strength increases as the complexity of the joint surface increases (Figure 18A). One possible explanation for the increased strength of the interdigitated joint is an increase in the coefficient of kinetic friction between the two surfaces under load (Alarcón *et al.*, 2016). This putative explanation could be verified by examining further interdigitated joints with different numbers of overlapping layers; if fewer layers result in a lower ultimate tensile strength this explanation is likely valid. This further understanding would enable more complex and easily customisable joints to be designed.

For interdigitated PETG-TPU the ultimate tensile strength obtained of 6.25 MPa ± 0.046 was comparable with the tensile strength of the enthesis of the extensor digitorum brevis: 14 MPa ± 9 reported by Morales-Orcajo *et al.* (2016). The extremely wide standard deviation reported by Morales-Orcajo *et al.* (2016) demonstrates the inter-subject variability of the strength of this interface.

Naturally, the anatomical location of an enthesis determines its strength. For instance, Abramowitch *et al.* (2010) report the proximal semitendinosus tendon of the lower limb has an ultimate tensile strength of 37.2 MPa ± 17.8 bears the weight of the whole body during locomotion. Whereas Kolz *et al.* (2015) describe the tendon of the long head of biceps brachii has an ultimate tensile strength of 22.3 MPa ± 9.3 as it only needs to support the weight of the forearm and any load it carries.

However, these results should be interpreted with caution. The solid samples failed at a lower tensile strength than was reported in the materials' data sheets (Ultimaker, 2022a; Ultimaker, 2022b; Ultimaker, 2022c). It is likely that this is due to the radius of the transition between the broad and narrow sections of the sample coupons being too small. Consequently, this concentrated the force in a smaller area than was calculated, resulting in artificially lower tensile stress values. It is also possible this difference is due to the inherent anisotropy in FDM, different infill densities and patterns than were used in the datasheets.

Moreover, the manufacturer's datasheets utilised a different standard to conduct tensile testing. The ASTM D3039 standard (American Society for Testing and Materials, 2017) used in these datasheets uses a test coupon of differing dimensions and shape to the one indicated by BS EN ISO 527-2:2012. Both standards calculate the engineering stress rather than true stress values, therefore this is not the reason for the differences observed. However, calculating the engineering stress ignores changes in the cross-sectional area of the sample, resulting in lower stress values.

Additionally, large deviations were present in the rates of extension used in this study compared to those suggested by the British Standard. However, this was a necessary alteration to be able to test the all of the samples in a timely manner. Moreover, BS EN ISO 527-2:2012 is designed for rigid materials which fail at a much lower strain than the elastomeric composites used here (Table 10); which are quicker to test at a given rate of strain than their elastomeric counterparts.

Given the magnitude of the effects of changing infill pattern and density of TPU 95A on its mechanical properties, there is scope to evaluate these parameters further in a multi-material setting. Testing of interdigitated PETG-TPU with different TPU infill densities and patterns may allow the design of samples with tensile properties in line with other entheses found in other anatomical locations.

Overall, the foundations laid here provide initial data for informed design of multi-material 3D printed models of the enthesis. Further optimisation of the interdigitated joint and slicing parameters present an attractive opportunity to tailor the tensile properties of the construct to more closely replicate those found in specific entheses.

Cytocompatibility

Indirect cytotoxicity testing revealed little difference between the materials employed in this project; all were equally non-cytotoxic to dRObs, as shown by the results obtained from each experimental group compared with the live controls.

The use of primary dRObs aids the generalisation of this work compared to use of immortalised cells lines. However, the high passage number is at the upper end of the longevity of these cells, possibly leading to genetic drift compared with cells that have spent less time in culture. Additionally, the use dRObs from a single batch leads to only technical replication being discussed herein. Future work using cells from a wider pool of sources would aid the generalisation of the effects reported here. To enhance the translatability of this work to the clinic the use of primary human osteteoblasts and tenocytes would be an intriguing project.

The lack of a control cell count for the trypan blue exclusion cell viability work severely limits its interpretation as results can only be compared with the number of seeded cells. Consequently, the cell death observed in culture cannot be definitively stated as an artifact of culture conditions or directly attributable to the materials used.

Overall, as mentioned throughout there are many under-powered experiments due to time and resource constraints. Future work would need *a priori* power analysis to determine statistically viable sample sizes to be used. However, data reported here provide a rich source of likely effect sizes to justify these estimations.

Kováčová *et al.* (2020) found PETG to have a mean contact angle of 86.9° ± 2.6 with a distilled water drop, indicating the droplet did not spread on the surface of the PETG due to its poor wettability. This result demonstrates PETG is in fact borderline hydrophobic, as defined by Förch *et al.* (2009) as a contact angle of 90° or more. This likely explains the poor adhesion of the cell suspension droplet in initial testing (Figure 24). Whilst it was initially confounding as to whether dRObs did not adhere to the disc or whether the droplet simply slid off. However, the addition of the lip seems to demonstrate cells will adhere to PETG when allowed sufficient time in contact with the disc (Figure 25).

Future work is needed to evaluate the cytocompatibility of these materials and tenocytes. This would be foundational to future use in a co-culture system with both osteocytes and tenocytes for entheseal tissue engineering.

Conclusion

Multi-material additive manufacturing can produce an anatomically relevant scaffold structure for possible future tissue engineering. Moreover, a combination of PETG and TPU with an interdigitated joint were found to have similar tensile properties to the extensor digitorum brevis of the human foot. Additionally, these materials were demonstrated to be compatible with dRObs *in vitro*. Ultimately, these results indicate an exciting possibility for use of multi-material 3D printing to produce rigid-compliant scaffolds for use in interfacial tissue engineering.

Reference List

Abramowitch, S. D., Zhang, X., Curran, M., Kilger, R. (2010). A comparison of the quasi-static mechanical and non-linear viscoelastic properties of the human semitendinosus and gracilis tendons. *Clinical Biomechanics,* 25**,** 325-331.

Alarcón, H., Salez, T., Poulard, C., Bloch, J.-F., Raphaël, É., Dalnoki-Veress, K., Restagno, F. (2016). Self-amplification of solid friction in interleaved assemblies. *Physical Review Letters,* 116**,** 015502-015502.

American Society for Testing and Materials (2017). *Standard test method for tensile properties of polymer matrix composite materials*, West Conshohocken: ASTM International.

Apostolakos, J., Durant, T. J., Dwyer, C. R., Russell, R. P., Weinreb, J. H., Alaee, F., Beitzel, K., Mccarthy, M. B., Cote, M. P., Mazzocca, A. D. (2014). The enthesis: A review of the tendon-to-bone insertion. *Muscles Ligaments Tendons J,* 4**,** 333-342.

Benjamin, M., Kumai, T., Milz, S., Boszczyk, B. M., Boszczyk, A. A., Ralphs, J. R. (2002). The skeletal attachment of tendons—tendon 'entheses'. *Comparative Biochemistry and Physiology Part A: Molecular & Integrative Physiology,* 133**,** 931-945.

British Standards Institution (2012). *BS EN ISO 527-2:2012. Plastics. Determination of tensile properties. Test conditions for moulding and extrusion plastics,* London: British Standards Institution.

British Standards Institution (2017). *BS EN ISO 37:2017. Rubber, vulcanized or thermoplastic — determination of tensile stress-strain properties,* London: British Standards Institution.

British Standards Institution (2019). *BS EN ISO 527-1:2019. Plastics. Determination of tensile properties. Part 1, general principles,* London: British Standards Institution.

Cormick, W. (2010). Enthesopathy – a personal perspective on its manifestations, implications and treatment. *Australasian Journal of Ultrasound in Medicine,* 13**,** 19-23.

Crowley, L. C., Scott, A. P., Marfell, B. J., Boughaba, J. A., Chojnowski, G., Waterhouse, N. J. (2016). Measuring cell death by propidium iodide uptake and flow cytometry. *Cold Spring Harbor protocols,* 2016**,** 647-651.

Czyrny, Z. (2012). Diagnostic anatomy and diagnostics of enthesal pathologies of the rotator cuff. *Journal of Ultrasonography,* 12**,** 178-187.

Drake, M. L. & Ring, D. C. (2016) Enthesopathy of the extensor carpi radialis brevis origin: Effective communication strategies. *Journal of the American Academy of Orthopaedic Surgeons,* 24**,** 365-369.

Faul, F., Erdfelder, E., Lang, A. G., Buchner, A. (2007) G*Power 3: a flexible statistical power analysis program for the social, behavioral, and biomedical sciences. *Behavior Research Methods,* 39**,** 175-191.

Förch, R., Schönherr, H., Jenkins, A. (2009) Appendix C: Contact angle goniometry. In: *Surface design: Applications in bioscience and nanotechnology,* pp. 471-473, edited by Förch, R., Schönherr, H., Jenkins, A. Weinheim: Wiley-VCH.

Khalilzadeh, O., Canella, C., Fayad, L. M. (2021) Wrist and hand. In: *Musculoskeletal diseases 2021-2024: Diagnostic imaging,* pp. 41-55, edited by Hodler J, Kubik-Huch RA, von Schulthess GK, Cham. Heidelberg: Springer International Publishing.

Kolz, C. W., Suter, T., Henninger, H. B. (2015) Regional mechanical properties of the long head of the biceps tendon. *Clinical Biomechanics,* 30**,** 940-945.

Kováčová, M., Kozakovičová, J., Procházka, M., Janigová, I., Vysopal, M., Černičková, I., Krajčovič, J., Špitalský, Z. (2020) Novel hybrid PETG composites for 3D printing. *Applied Sciences*, pp. 3062.

Morales-Orcajo, E., Becerro De Bengoa Vallejo, R., Losa Iglesias, M., Bayod, J. (2016) Structural and material properties of human foot tendons. *Clinical Biomechanics,* 37**,** 1-6.

Mortimer, J. W., Alsaykhan, H., Vadibeler, S., Rust, P. A., Paxton, J. Z. (2021) Anatomy and histomorphology of the flexor digitorum profundus enthesis: functional implications for tissue engineering and surgery. *BMC Musculoskeletal Disorders,* 22**,** 1032.

R Core Team (2022) R: A language and environment for statistical computing. Vienna, Austria: R Foundation for Statistical Computing.

Ruchelsman, D. E., Christoforou, D., Wasserman, B., Lee, S. K., Rettig, M. E. (2011) Avulsion injuries of the flexor digitorum profundus tendon. *Journal of the American Academy of Orthopaedic Surgeons,* 19**,** 152-162.

Schindelin, J., Arganda-Carreras, I., Frise, E., Kaynig, V., Longair, M., Pietzsch, T., Preibisch, S., Rueden, C., Saalfeld, S., Schmid, B.*, et al.* (2012) FIJI: An open-source platform for biological-image analysis. *Nature Methods,* 9**,** 676-682.

Stansbury, J. W. & Idacavage, M. J. (2016) 3d printing with polymers: Challenges among expanding options and opportunities. *Dental Materials,* 32**,** 54-64.

Uggeri, J., Gatti, R., Belletti, S., Scandroglio, R., Corradini, R., Rotoli, B. M., Orlandini, G. (2000) Calcein-AM is a detector of intracellular oxidative activity. *Histochemistry and Cell Biology,* 122**,** 499-505.

Ultimaker (2022a), Ultimaker ABS technical data sheet, https://makerbot.my.salesforce.com/sfc/p/j0000000HOnW/a/5b000004UWOb/mqEDmbBEqiM6dfNicGFkHQEgcV9T8W762bqwplt4bxo [Accessed: 21/04/2023].

Ultimaker (2022b), Ultimaker PLA technical data sheet, https://makerbot.my.salesforce.com/sfc/p/j0000000HOnW/a/5b000004UiRV/lt4XCkl0KOSLfPMcyG06mKKbES33WnYiFrMsG8bFGhw [Accessed: 21/04/2023].

Ultimaker (2022c), Ultimaker Tough PLA technical data sheet, https://makerbot.my.salesforce.com/sfc/p/j0000000HOnW/a/5b000004UgTE/z40nDBo3Clypj7u9xI7MbeVe.CNpDM_Mq0nhvbpyne8 [Accessed: 21/04/2023].

Vesvoranan, O., Anup, A., Hixon, K. R. (2022) Current concepts and methods in tissue interface scaffold fabrication. *Biomimetics,* 7**,** 151.

Wickham, H. (2016) *Ggplot2: elegant graphics for data analysis.,* New York, USA: Springer-Verlag.

Wood, S. N. (2011) Fast stable restricted maximum likelihood and marginal likelihood estimation of semiparametric generalized linear models. *Journal of the Royal Statistical Society: Series B (Statistical Methodology),* 73**,** 3-36.

Wood, S. N. (2016) *Generalized additive models: an introduction with R,* Boca Raton: Chapman & Hall/CRC.